Acta Geotechnica (2018) 13:575–599
https://doi.org/10.1007/s11440-017-0560-2

RESEARCH PAPER

Multiscale modeling and analysis of compaction bands in high-porosity sandstones

Huanran Wu[1] · Ning Guo[1] · Jidong Zhao[1,2]

Received: 17 October 2016 / Accepted: 2 May 2017 / Published online: 24 May 2017

Abstract We present a multiscale investigation on the initiation and development of compaction bands in high-porosity sandstones based on an innovative hierarchical multiscale approach. This approach couples the finite element method and the discrete element method (DEM) to offer direct, rigorous linking of the microscopic origins and mechanisms with complex macroscopic phenomena observed in granular rocks such as strain localization and failure. To simulate compaction band in granular cementitious sandstone, we adopt a bonded contact model with normal and tangential interparticle cohesions in the DEM and propose a dual-porosity structure consisting of macropores and interstitial voids for the representative volume element to mimic the typical meso-structure of high-porosity sandstones. In the absence of particle crushing, our multiscale analyses identify debonding and pore collapses as two major contributors to the formation of compaction bands. The critical pressures predicted by our simulations, corresponding to surges of debonding and pore collapse events, agree well with the estimations from field data. The occurrence patterns of compaction band are found closely related to specimen heterogeneity, porosity and confining pressure. Other deformation band patterns, including shear-enhanced compaction bands and compactive shear bands, were also observed under relatively low confining pressure conditions with a rough threshold at $0.55P^*$ (P^* is the critical pressure) on the failure envelop. Key microscopic characteristics attributable to the occurrence of these various deformation patterns, including fabric anisotropy, particle rotation, debonding and pore collapse, are examined. Shear-enhanced compaction bands and pure compaction bands bear many similarities in terms of these microscopic characteristics, whereas both differ substantially from compactive shear bands.

Keywords Compaction bands · Coupled FEM and DEM · Microstructure · Multiscale modeling · Porous sandstone · Strain localization

1 Introduction

Deformation bands are widely observed in both laboratory and natural conditions in sandstone. They may present in rich forms ranging from localized shear band, compaction or dilatant band to various hybrid patterns of them [5]. Deformation bands typically attract concentrated deformation occurred to a sandstone. A thorough understanding of their occurrence and formation mechanisms is critical to the design and operation of relevant structures, including oilfield boreholes, natural terrain slopes and regional aquifer system. While shear bands have been well investigated over the past decades by means of field and laboratory testing and theoretical modeling [3, 9, 26, 49], other deformation patterns entered the recent spotlights for geophysics and geomechanics researchers, among which compaction bands have received special attention.

A compaction band occurs in sandstones in forms of tabular zones with pure compaction deformation and little or no shear, which uniquely distinguishes it from a shear band. Field observations of compaction bands have been reported in the Jurassic Navajo Sandstone in Utah, USA

✉ Jidong Zhao
jzhao@ust.hk

[1] Hong Kong University of Science and Technology, Clearwater Bay, Kowloon, Hong Kong

[2] HKUST Shenzhen Research Institute (SRI), Shenzhen, China

[25, 49, 62], and the Jurassic Aztec Sandstone in Nevada, USA [4, 21, 33, 63]. The presence of compaction band has been found to cause a dramatic reduction in both porosity and permeability within compaction bands as compared to the host rock [25] and hence can significantly alter the flow in rocks, leading to great challenges for practical applications in oil/gas storage and extraction, CO_2 sequestration, nuclear waste disposal and aquifer management [20, 34, 57].

The formation of compaction bands in high-porosity sandstones has been investigated under a variety of laboratory testing conditions, including triaxial compression tests on cylindrical samples [22, 40, 54, 66, 72, 74] and specimens with V-shaped [64] or round-ended notches [11, 12, 67] as triggers. The effect of the intermediate principal stress (σ_2) has been examined by true triaxial experiments on cuboidal specimens [43]. The slot-shaped breakouts around boreholes observed in laboratory drilling tests by Katsman et al. [38] have been considered as the formation of compaction bands too. Major similarities and differences between compaction bands and other deformation patterns, such as shear bands and shear-enhanced compaction bands, have also been examined [11, 12, 23]. Collectively, these experiments have shown that the formation of compaction bands requires a relatively high porosity for the specimen (13–28%) and depends crucially on other important factors including the homogeneity of the host rock, the confining pressure, the rock mineralogical composition, the presence of cement and the grain size distribution [14, 34, 65].

There have been considerable advances in theoretical and numerical investigations of compaction bands. The bifurcation theory [61], which was originally developed for analyzing shear bands, has been successfully extended to determine the onset condition and the orientation of a compaction band [10, 54, 60, 74]. To describe the evolution and/or extension of the compaction band beyond its inception, theoretical models similar to fracture mechanics have been developed to treat stress concentration around physical inclusions in various forms, such as a contractile ellipsoid, an anti-crack or a localized reduced volume [37, 49, 63]. These inclusions can induce inhomogeneous deformations and guide the subsequent development of compaction band. These theoretical models prove to be useful in modeling and predicting compaction bands in a boundary value problem when they are implemented into the finite element method (FEM) [53]. More recently, the emerging discrete element method (DEM) based on micromechanics of granular materials has also been successfully applied to simulate compaction bands in cohesive porous sandstones. Marketos and Bolton [44–46] investigated the occurrence of discrete/diffuse compaction bands due to grain crushing and debonding based on DEM simulations. In considering intra-granular damage, Wang et al. [68] modeled different types of compaction bands by shrinking the sizes of crushed particles. Without considering particle breakage in their DEM, Dattola et al. [18] argued that the macro-pores could also trigger the formation of compaction bands. Other micro-mechanics-based approaches, such as the spring network model, have also been used to model compaction bands in sandstones [16, 17, 37].

Despite the aforementioned progresses, many related issues on compaction band are still open to debate. In particular, the compaction bands in laboratory experiments have usually been observed at a high confining pressure level in the magnitude of 100 MPa [6, 12, 22], a value rather close to the stress state when a geomaterial typically undergoes brittle–ductile transition [10, 60]. At this stress level, grain crushing is regarded as the major contributor to the formation of compaction bands. However, as argued by Sternlof et al. [63], the natural compaction bands commonly occur in poorly cemented sandstones at moderate mean compressive stress levels. The critical pressure for the formation of compaction bands estimated from field observations is only around 20 MPa [21, 25, 62, 63]. Indeed, both the stress level and the degree of grain crushing in field observations are much lower than those reported in the laboratory tests. In addition, discrete compaction bands are found in field investigations and are interlayered by largely undamaged zones [25, 49], whereas the compaction fronts in most laboratory experiments or numerical simulations have been found to propagate from the ends to the center of the specimen [6, 35]. Since the length scale in the laboratory is small and the tested specimens are relatively homogeneous, the heterogeneities in the field are believed to be responsible for the resultant different patterns of compaction bands [22, 23].

This study aims to investigate relevant issues on compaction bands from a multiscale perspective. In sandstone, a wide range of microstructures and mechanisms can serve as triggers for compaction band and other deformation bands, including heterogeneously distributed big pores and weakly cemented interparticle bonds. The identification of key microstructures and their unique or combined roles in dictating the inception and formation of compaction band may potentially help resolve relevant puzzles mentioned above and improve our fundamental understanding of this important phenomenon. To this end, a hierarchical multiscale approach originally developed by Guo and Zhao [27] will be adopted. In this multiscale approach, FEM is used to solve a boundary value problem and at each Gauss point of the FEM mesh, a representative volume element (RVE) is embedded, receives the deformation gradients as its boundary conditions and is solved by DEM simulations to derive the local material constitutive responses required for advancing the FEM computations (see Fig. 1). This

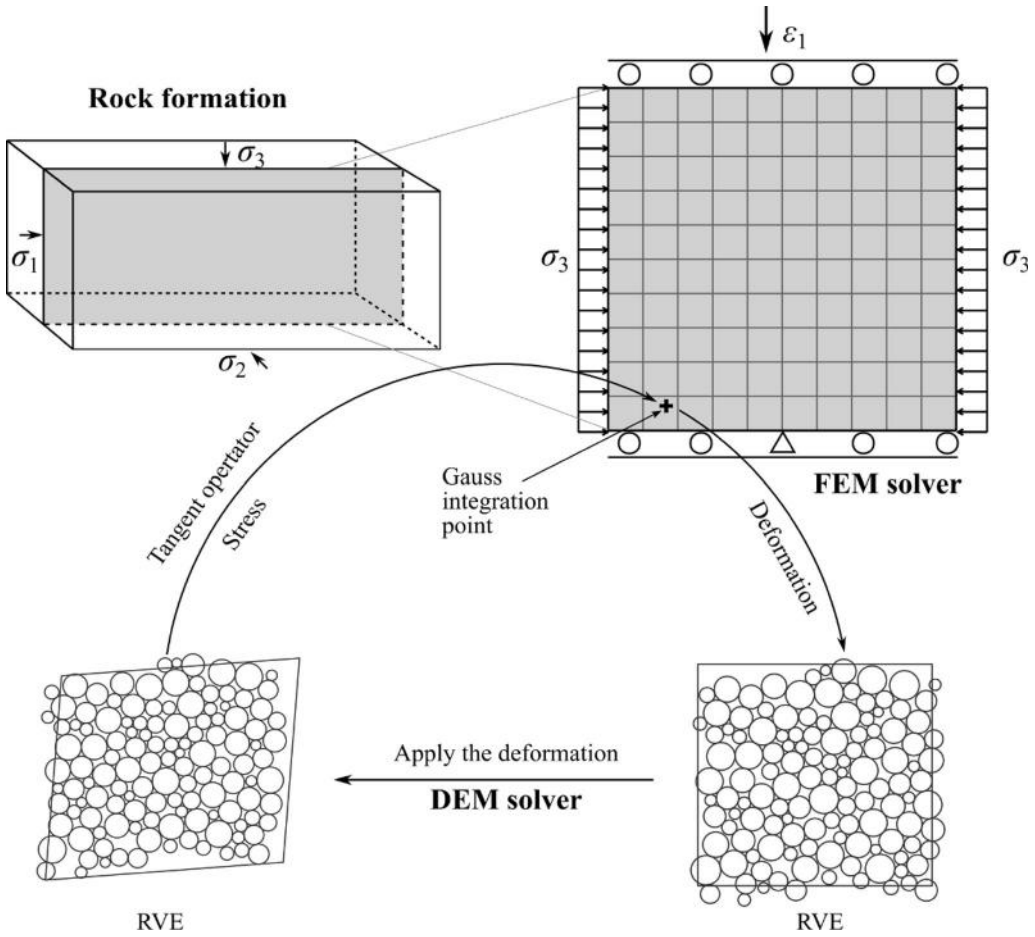

Fig. 1 Illustration of the solution procedure for the coupled FEM/DEM hierarchical multiscale modeling approach in solving a boundary value problem for sandstone

approach hence features both the efficiency of conventional FEM in modeling the structural responses and the exemption of needs of phenomenological constitutive assumptions as in conventional approaches. It can also facilitate direct cross-scale analyses for macro–micro-transition problems, a key focus to be highlighted in the present study. The approach has been successfully applied to simulate shear bands in anisotropic soils [76] and the failure of various geostructures, such as retaining wall, footing and wellbore [29, 31]. Similar approaches have also been reported elsewhere, such as Meier et al. [47], Andrade et al. [1], Miehe et al. [48], Nitka et al. [51], Nguyen et al. [50] and Liu et al. [42]. The following sections will demonstrate that this multiscale approach is effective in simulating the behavior relevant to compaction bands in porous sandstones and is convenient to examine the evolution of local microstructural attributes, such as fabric anisotropy, particle rotation, debonding and pore collapse, during the evolution of a compaction band. This study may thus offer a fresh multiscale perspective toward understanding the complex phenomena of compaction bands.

2 Hierarchical multiscale modeling of compaction bands

As illustrated in Fig. 1, the coupled FEM/DEM multiscale modeling approach uses a two-way interactive RVE to replace the conventional phenomenological constitutive model required at each Gauss integration point in a continuum-based FEM. On the one hand, the RVE receives the deformation from the FEM at the corresponding Gauss point as boundary/loading conditions, and as a return, it feedbacks the FEM with updated tangent operator and stress at the Gauss point to advance the FEM calculation. Central to the multiscale approach is the preparation of a RVE packing to embed at each Gauss point of the FEM mesh to derive the local material constitutive responses. The following summarizes how a typical RVE is prepared to represent the high-porosity structure of sandstone and to

produce its typical mechanical behaviors observed in laboratory tests. The readers can refer to Guo and Zhao [27] for detailed formulations and solution algorithms of the coupled FEM/DEM hierarchical multiscale approach which will not be repeated here.

2.1 RVE preparation

A simple bonded contact model is used to replicate the behavior of cohesive sandstone. We further develop an innovative procedure to generate a dual-porosity structure for each RVE packing to represent the typical porous structure of sandstones. For conceptual simplicity and computational efficiency, we elect to demonstrate it for two-dimensional (2D) analyses, and its 3D extension is straightforward (see, for example, [28]).

2.1.1 Bonded contact model

There have been ample experimental data and simulating results devoted to the understanding of cohesive granular materials. For example, Delenne et al. [19] had performed an experimental study on glued aluminum rods to investigate the bond behavior as a reference for their DEM models. Potyondy and Cundall [59] had introduced a parallel-bond model considering both contact force and moment, which has been widely adopted to simulate the behavior of cemented sand [70] and rock [39]. A simplified version of the bonded contact model, without considering contact moment and hence requiring fewer parameters, has also been successfully applied to simulate crushable agglomerates [13] and rocks with joints [58]. This simplified bonded contact model is adopted in the current study. The contact model employs a linear force–displacement contact law and a Coulomb-type friction criterion. The normal and the tangential contact stiffnesses can be obtained from the following equations

$$k_{\mathrm{n}} = E_{\mathrm{c}} r^{*} \tag{1}$$

$$k_{\mathrm{t}} = v_{\mathrm{c}} k_{\mathrm{n}} \tag{2}$$

where $r^{*} = 2r_1 r_2/(r_1 + r_2)$, r_1 and r_2 are the radii of the two contacted particles. E_{c} and v_{c} are two user-defined parameters. At each contact, normal and tangential contact bonds are assigned according to the following expressions

$$a_{\mathrm{n}} = C_{\mathrm{n}} \min(r_1, r_2)^2 \tag{3}$$

$$a_{\mathrm{t}} = C_{\mathrm{t}} \min(r_1, r_2)^2 \tag{4}$$

where C_{n} and C_{t} are the normal and the tangential cohesion strengths, respectively. The breaking of a bond is governed by either the maximum tensile force $F_{\mathrm{n}}^{\max}$ (specified by a_{n}) for tension failure, or a threshold for tangential force $F_{\mathrm{t}}^{\max}$ ($F_{\mathrm{t}}^{\max} = a_{\mathrm{t}} + F_{\mathrm{n}} \tan\phi$, where ϕ is the interparticle friction angle) for shear failure. When either of the two thresholds is exceeded, the bond is considered to be broken and will be eliminated, leaving a pure frictional contact after bond breakage. A pure frictional contact without bond is governed by the Coulomb's friction law (e.g., $F_{\mathrm{t}} \leq F_{\mathrm{n}} \tan\phi$). The normal and the tangential force–displacement relationships for the contact model described above are illustrated in Fig. 2.

The microscopic parameters adopted for generating the RVE packing are summarized in Table 1. These values are typically used in DEM models for sands and sandstones [27, 46, 68]. Grain size distribution plays an important role in the mechanical response of a granular material. Indeed, a good sorting has been observed in the sandstone which formed compaction bands in the field [2]. Based on a systematic experimental study of sandstones with different gradings, Cheung et al. [14] had concluded that discrete compaction bands were favored in the well-sorted specimens. The effect of grain size distribution has also been confirmed in DEM simulations of compaction band in sandstone [68]. Hence, a grain size distribution with radii uniformly ranging from 4 to 6 mm is adopted in this study. The mean values of C_{n} and C_{t} are set to be equal to 5 GPa, following the recommendation by Wang and Leung [70] and Wang et al. [68] for cemented sand and sandstones. In addition, small variations of the cohesion strength are allowed to introduce material heterogeneity.

2.1.2 Dual-porosity structure

Intense grain crushing has been found in compaction bands observed in laboratory experiments on sandstone [6, 12, 22]. To examine the effect of particle breakage, various techniques have been attempted in past DEM studies on compaction band, including total removal of the broken grains, shrinking the size of the crushed grains, softening the broken grains or replacing them with several smaller ones [46, 68]. While the community has paid considerable attention to key role played by particle crushing, field observations appear to indicate much fewer and significantly less severe grain damage in compaction bands found in the field [4, 63] than those reproduced in the laboratory. The apparent contradiction has drawn wide interests for the community toward a fuller investigation on the differences pertaining to the occurrence and formation of compaction bands in laboratory and field conditions as well as a careful rethinking of the role played by particle crushing in compaction bands [63].

Key questions aroused by the contradictory observations include, but not limited to, whether there are other dominant factors/mechanisms contributing to the occurrence of compaction bands in the absence of particle crushing. Indeed, Dattola et al. [18] had recently confirmed the

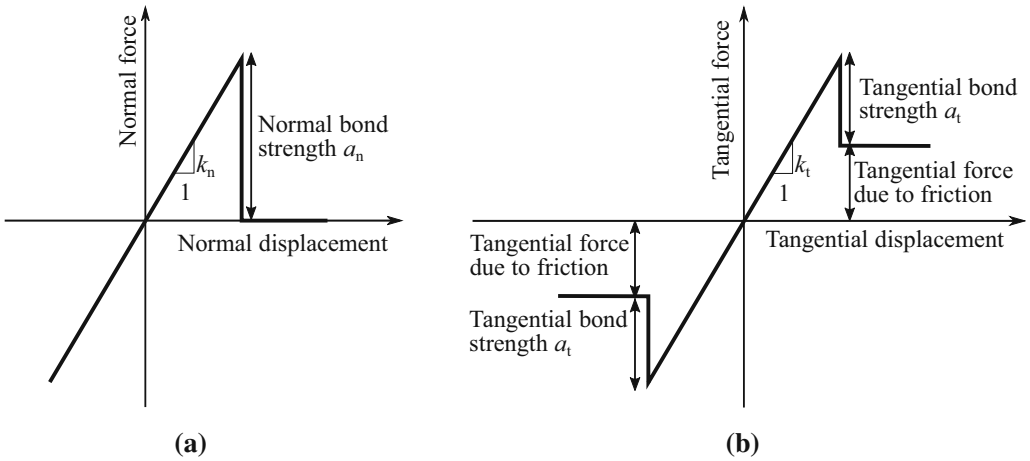

Fig. 2 **a** Normal and **b** tangential force–displacement relationships for the bonded contact model

Table 1 Parameters for the RVE

Radii r (mm)	Density ρ_p (kg/m^3)	E_c (GPa)	ν_c	Friction angle ϕ (°)	C_n, C_t (GPa)
4–6	2650	88	0.8	30	5

formation of compaction band without particle crushing in an idealized material with a dual-porosity structure. The dual-porosity structure they employed was abstracted from the structure observed in highly porous calcarenite with macro-intercluster pores and general micro-interparticle voids [15]. Similar structure has been reported in sandstones where the macro-pores present a shape and a size resembling that of grains. These grain-shaped pores may have been formed due to the weathering out of feldspar grains or other processes [11]. The foregoing studies demonstrate that, without necessary involvements of particle breakage, the presence of dual-porosity structure in sandstone could cause intense porosity reduction due to macro-pore collapse. The present study aims to further testify this argument from a multiscale viewpoint, in attempting to reconcile the contradictory observations on particle crushing in field and laboratory compaction bands.

Typical RVE packing with dual-porosity structure used for the subsequent multiscale modeling has been prepared according to the following procedures:

(1) A random packing of 800 spherical particles containing uniformly distributed radii ranging from 4 to 6 mm is generated. Among these particles, 2% are larger ones (with a typical radius of 15 mm) for later removal to produce macro-pores.
(2) The generated packing is then isotropically compressed to 90% of the target confining pressure. A larger frictional coefficient is assigned to produce a loose packing, and a smaller value for a dense packing. The typical packing at the end of this stage is illustrated in Fig. 3a.
(3) Normal and tangential cohesions are applied to interparticle contacts in the packing, in an analogous manner to the natural cementation process [7]. The larger particles and the rattlers (particles with only or less than one contact) are then removed from the packing to generate a dual-macro–micro-porosity structure. A packing with the remaining 693 particles are illustrated in Fig. 3b, wherein the macro-pores are depicted as the voids left by the removed larger particles and the rest are micro-pores within the original packing.
(4) The packing is further isotropically consolidated to reach the target confining pressure. Cohesion is reapplied to the interparticle contacts to ensure an initially intact packing. The final packing achieved by the above procedures is illustrated in Fig. 3c. The porosity of the shown type A RVE packing after isotropic consolidation under 10 MPa is 0.380.

2.2 Biaxial compression tests

A square specimen with a side length of 50 mm, shown in Fig. 4, is considered. Eight-noded serendipity elements are used with four Gauss points for each element (reduced integration). The generated RVE with dual-porosity

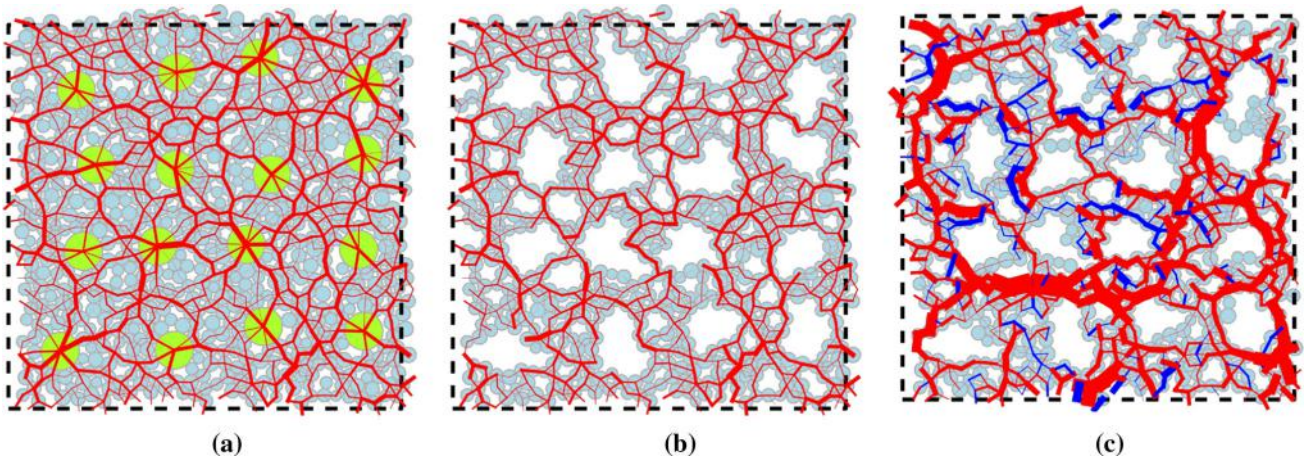

Fig. 3 Preparation of a RVE (type A in Table 2) with dual-porosity structure for multiscale modeling of sandstone. Stage **a**: initial packing after 90% isotropic consolidation. Stage **b**: packing after adding interparticle cohesion and removal of large particles and rattlers. Stage **c**: final packing after full consolidation with dual-porosity structure. Lines in the figures indicate interparticle normal contact forces where the line thickness is proportional to force magnitude. Color interpretation for contact force: *red* for compressive contacts and *blue* for tensile contacts (color figure online)

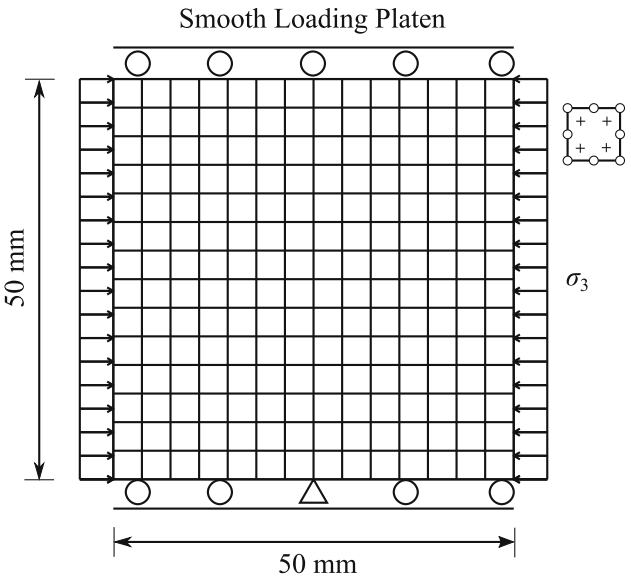

Fig. 4 FE discretization by eight-noded serendipity elements of four Gauss points and the prescribed boundary conditions for biaxial compression tests on a square specimen

structure is then attached to each Gauss point of the finite element mesh. Regarding the choice of specimen shape, an aspect ratio of 2 has been commonly used in the laboratory to reduce the boundary effect, i.e., the influence of friction between the ends of the specimen and the loading platens. This is not an issue in the numerical test with ideal smooth boundary conditions. Thus, an aspect ratio of 1 is used in the study to reduce the computational cost and to avoid possible deflection of the specimen when it is subjected to biaxial compression loadings. Notably, Bésuelle et al. [9] indeed have observed a similar localization pattern in specimens with aspect ratios of both 1 and 2.

The tectonic stress in the field is usually complex with distinctive principal stress components (e.g., $\sigma_1 > \sigma_2 > \sigma_3$), which differs essentially than the conventional triaxial stress condition tested for compaction bands in the laboratory ($\sigma_1 > \sigma_2 = \sigma_3$) [22, 54, 66, 74]. Indeed, Issen and Rudnicki [36] had concluded that the conventional triaxial configuration is the most favorable deviatoric stress state for the formation of compaction bands. Meanwhile, there have been extensive both experimental and numerical modeling of biaxial compression tests to study compaction bands and brittle–ductile transitions [41, 68, 77], due to easy model setup and interpretation. In this study, we hereby choose monotonic biaxial compression tests as the testing condition for compaction band.

To reflect the inhomogeneous nature of sandstone, we follow Hazzard et al. [32] and set the cohesion strength C_n and C_t, for different RVE packings at different Gauss points to obey the Gaussian distribution. In laboratory tests, compaction bands have been observed to nucleate at some spots of high porosity and spread laterally across the sample [22]. The spots with lower cohesion strength for the generated packings here, namely the local weak points, are expected to play a similar role acting as the nuclei for the initiation of compaction bands. The variable $C_{\blacksquare}$, where the subscript '$\blacksquare$' denotes either n or t, after normalization via $(C_{\blacksquare} - \bar{C}_{\blacksquare})/(c_v \cdot \bar{C}_{\blacksquare})$, is assumed to obey the standard normal distribution, where $\bar{C}_{\blacksquare}$ is the mean cohesion strength and c_v is the coefficient of variation (standard deviation divided by mean). The probability density of the normalized cohesion strength and its spatial distribution over the problem domain are shown in Fig. 5. A standard normal distribution can be observed for the normalized cohesion strength in Fig. 5a. The coefficient of variation c_v

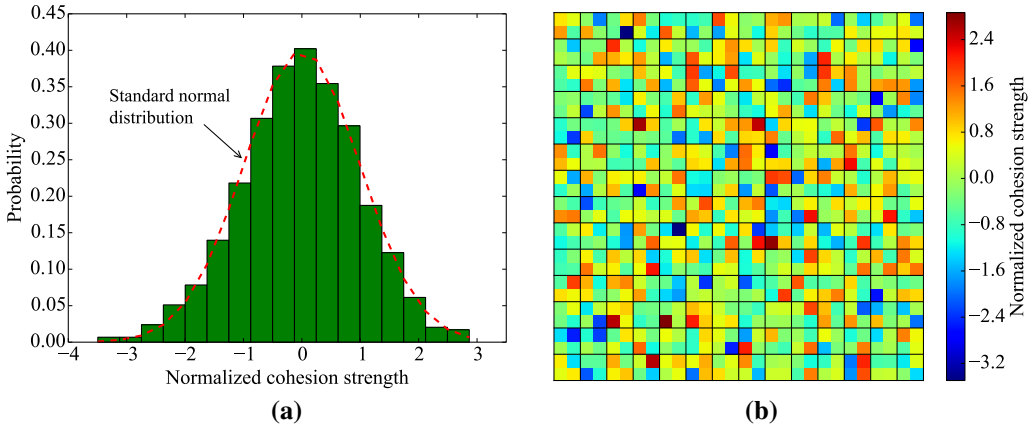

Fig. 5 **a** Probability distribution and **b** spatial distribution of the normalized cohesion strength $(C_{\blacksquare} - \bar{C}_{\blacksquare})/(c_v \cdot \bar{C}_{\blacksquare})$

can be used to measure the degree of heterogeneity for the specimen. In the study, c_v is set to be the same for both C_n and C_t.

3 Modeling of pure and shear-enhanced compaction bands and compactive shear bands

To investigate the effect of concerned factors, including confining pressure, heterogeneity, porosity, we conducted 13 biaxial compression tests as summarized in Table 2. Notably, it is not possible for all relevant factors to be discussed in one study. Hence, the effects of other factors, such as temperature and strain rate, are not considered here. We prepared two types of RVE (A and B) with different microstructures to investigate the effect of porosity. Within each type of RVE, slight variations of porosity and contact number may exist due to the difference in confining pressure, while the overall microstructure remains largely the same. In terms of heterogeneity, three kinds of specimens are considered, namely the homogeneous one, the one with two weak points at its center and the one with normal distributed cohesion strength. The last column of the table also summarizes the observed failure patterns by our multiscale simulations to be shown in the following.

3.1 Pure compaction bands

Compaction bands were reported in laboratory tests to occur at a critical state characterized by the onset of grain crushing and pore collapse. The critical pressure under hydrostatic loading is approximated by $P^* \propto (nR)^{-1.5}$, where n is the porosity and R is the average grain size [75]. Most of the reported critical pressure in laboratory is in the magnitude of 100 MPa [65, 71, 75]. This value is substantially higher than that observed in the field of the Jurassic Navajo Sandstone which has been estimated to be around 20 MPa [62]. Moreover, the effective stress field for the compaction bands in Aztec Sandstone at Valley of Fire is inferred to be $\sigma_1 \sim 22$ MPa and $\sigma_3 \sim 7$ MPa [21]. The present study selects a confining pressure at 10 MPa for pure compaction band case to be more consistent with the field observation (please refer to Case I in Table 2 for detailed setup).

How the cohesion strength varies in a natural material remains a challenge due to the difficulty in measuring its value by available laboratory means. A small value of $c_v = 0.05$ is used, which helps induce the nucleation of compaction bands from our parametric study. In the following presentation, compression is treated as positive. The major and the minor principal stresses, in the vertical and the horizontal directions, are denoted by σ_1 and σ_3, respectively. The mean effective stress is given by $p = (\sigma_1 + \sigma_3)/2$ and the deviatoric stress by $q = \sigma_1 - \sigma_3$ for a 2D study.

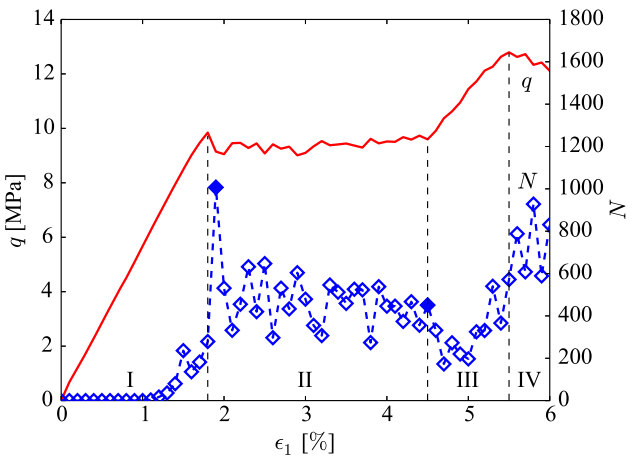

Fig. 6 Evolution of global deviatoric stress and debonding number with ϵ_1

3.1.1 Global response and debonding

Figure 6 presents the evolutions of the global deviatoric stress q and the debonding number N (summed over the whole domain) with the axial strain ϵ_1 during the compression of the specimen. Our multiscale modeling results show qualitative agreements with the experimental data for Castlegate [56] and Bentheim sandstones [6]. As shown in Fig. 6, the stress–strain relationship is evidently characterized by the following four stages, bounded by dashed vertical lines in the figure.

(1) A steep linear increase in q with strain is observed during the first stage, indicating a largely elastic behavior accompanied by negligible debonding events. Debonding becomes notably active only when the first peak in q is approached.
(2) After the first peak, a slight decrease in q is observed followed by a nearly constant plateau with mild fluctuations. This stage corresponds to the initiation and formation of compaction bands associated with a burst of debonding events. As demonstrated in Fig. 7b–d, the compaction bands initiate from the weak points and propagate mainly in the horizontal direction as well as expand slightly in the vertical direction. At the end of this stage, the whole specimen is densified due to cumulative pore collapse.
(3) With continuous loading, the shear stress picks up its linear increase with the strain again during the third stage. Nevertheless, the slope (stiffness) is apparently smaller than that in the first stage, due to the debonding processes that have happened in the material.
(4) After reaching a second higher peak for q, a softening response is observed at the fourth stage. This is a typical shear softening process for frictional materials during which shear banding localization may happen (but will not constitute a focus of this study). The simulation was terminated at $\epsilon_1 = 6\%$. The above observations are consistent with the predictions based on continuum elasto-plasticity models [36, 54].

Acoustic emission (AE) has been widely used to examine the damage progress in a specimen in experiments. An AE event represents a micro-mechanical failure event involving particle crushing, debonding and/or pore collapse [23]. Since particle crushing has not been considered in the study, debonding was recorded during our simulations to serve as an indicator of micro-damages (see also in Zheng et al. [77]). As shown in Fig. 6, at the beginning of stage II, the stress drop is associated with a drastic increase in debonding number, with N reaching a peak at the end of the stress drop. The peak of N corresponds to a dramatic horizontal spread of compaction bands, which will be discussed in detail later. The process is similar to the spatial clustering of damage zones spreading perpendicular to the major principal stress direction reported in experimental triaxial compression tests of Bentheim, Rothbach and Berea sandstones [6]. During the second stage, the episodic fluctuation of N and the plateau with mild fluctuation of q show a similar trend to experimental observations on the Bentheim sandstone where discrete compaction bands were found with the so-called "p-type" AE activities [6].

3.1.2 Propagation of compaction bands

The initiation and development of compaction bands are too complicated to be characterized by a single variable. We use a combination of three variables for the characterization, namely the global distributions of volumetric strain (ϵ_v) and the deviatoric strain (ϵ_q) for identifying the initiation of compaction bands, and the local debonding number (N), comparable to AE rate, as an indicator of damage process during the propagation of compaction bands. To obtain the strain information of each RVE, accumulated infinitesimal strain tensor $\boldsymbol{\epsilon}$ is calculated from the symmetric part of the boundary displacement gradient $\nabla \mathbf{u}$ at the corresponding Gauss point (obtained from the FEM solution). The volumetric strain ϵ_v and the deviatoric strain ϵ_q are defined as follows

$$\epsilon_v = -\mathrm{tr}\boldsymbol{\epsilon} \tag{5}$$

$$\epsilon_q = \sqrt{2\boldsymbol{e}:\boldsymbol{e}} \tag{6}$$

where 'tr' indicates the trace of the tensor; ':' denotes the double contraction between two tensors; and $\boldsymbol{e}$ is the deviatoric strain tensor.

The contours of ϵ_v, ϵ_q and N at different axial strain levels are illustrated in Fig. 7. Noticeable debonding events are observed at $\epsilon_1 = 1.1\%$(c.f. Fig. 6) at the weak points, and then spread over the specimen through relatively weak points with increasing load. The spread of debonding yields the first small peak in the N–ϵ_1 curve at $\epsilon_1 = 1.5\%$ (c.f. Fig. 6). At this stage, the whole sample could be still regarded as intact and the q–ϵ_1 curve is almost linear. The debonding number is so small that it does not change the global stress–strain relationship or influence the overall structure stability. At $\epsilon_1 = 1.8\%$, a yield point is observed in the q–ϵ_1 curve, marking the end of the pure elastic compression stage. Apparent concentrated spots of ϵ_v, ϵ_q and N are observed in Fig. 7a, showing similar localization patterns for the three measures.

As the loading further continues, the debonding number dramatically increases right after the yield of the specimen, leading to a peak for N at $\epsilon_1 = 1.9\%$ (c.f. Fig. 6). The localization patterns of ϵ_v, ϵ_q and N are illustrated in

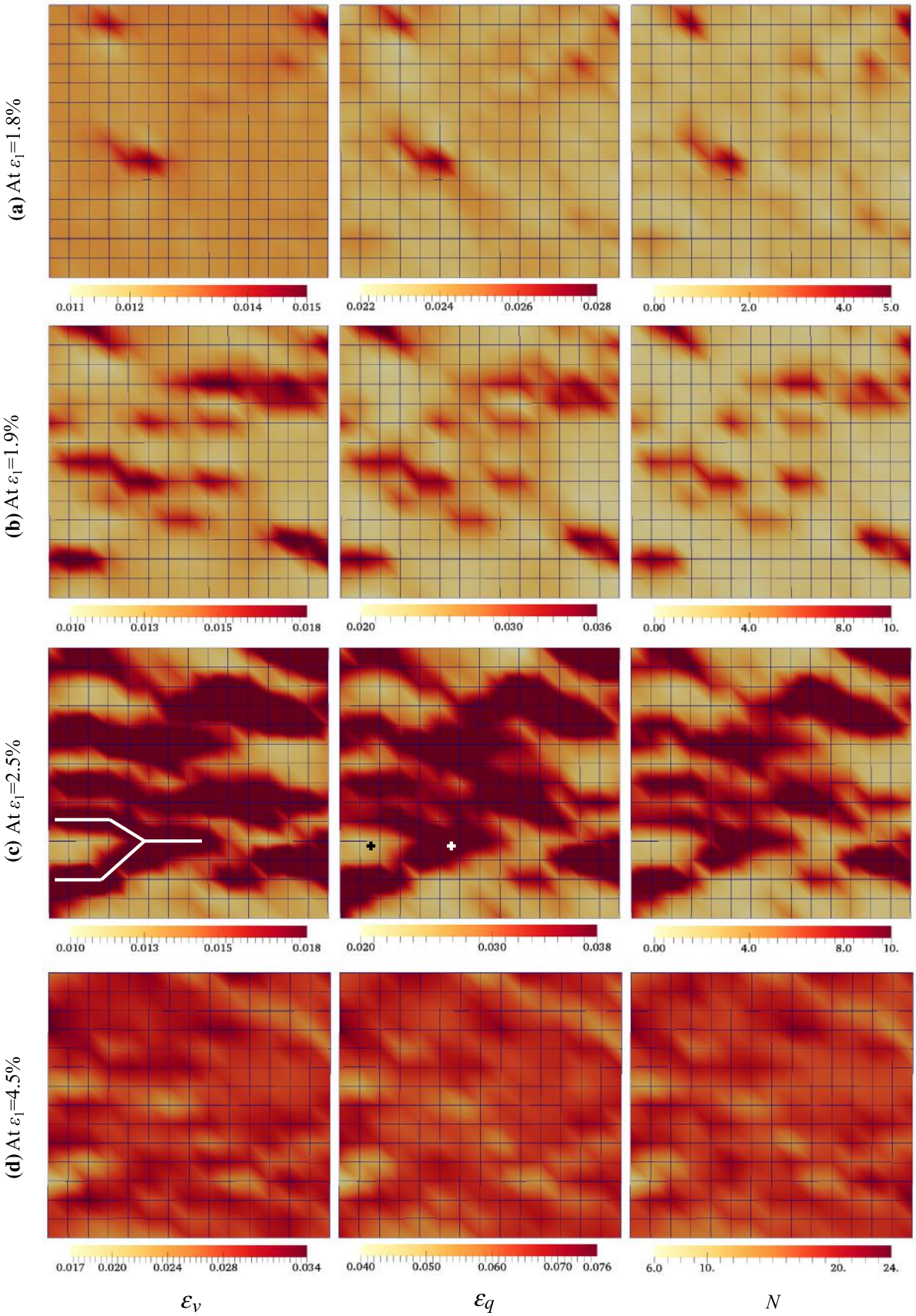
(a) At ε_1=1.8%
(b) At ε_1=1.9%
(c) At ε_1=2.5%
(d) At ε_1=4.5%
0.011 0.012 0.014 0.015
0.022 0.024 0.026 0.028
0.00 2.0 4.0 5.0
0.010 0.013 0.015 0.018
0.020 0.030 0.036
0.00 4.0 8.0 10.
0.010 0.013 0.015 0.018
0.020 0.030 0.038
0.00 4.0 8.0 10.
0.017 0.020 0.024 0.028 0.034
0.040 0.050 0.060 0.070 0.076
6.0 10. 20. 24.
ε_v
ε_q
N

◀**Fig. 7** Contours of ϵ_v (volumetric strain), ϵ_q (deviatoric strain) and N (debonding number) at different axial strain levels (marked in sequence as *empty circles* in Fig. 6) during the formation of compaction bands (Case I in Table 2)

Fig. 7b, where the contours indicate the localization bands spread nearly horizontally from the weak points. The volumetric strain of these damaged regions increases steadily, forming the early stage compaction bands. Similar pronounced planar localizations of AE hypocenters have been reported during the formation of discrete compaction bands in Bleurswiller sandstone [22]. Clearly, the initiation of compaction bands in the simulated sandstone coincides with the beginning of the inelastic compression. The weak material points act as the nuclei of the compaction bands extending toward the horizontal direction. This pattern of development has indeed been verified by theoretical models considering an anti-crack inclusion or a local weak point as inhomogeneity to trigger compaction bands [37, 49, 63].

After the initiation stage, the first localization continues to spread in the horizontal direction, while several other interlayered compaction bands are subsequently formed (Fig. 7c). This stage corresponds to the plateau of the q–ϵ_1 curve. During this stage, N fluctuates dramatically as shown in Fig. 6 where each spike of N represents a surge of debonding and corresponds to a small drop of q in the q–ϵ_1 curve. It is found that the surge of debonding occurs predominantly along with the spreading pathway of the compaction bands in the horizontal direction, while other parts of the specimen exhibit little or no damage as shown in Fig. 7b, c. Similar unstable propagation of discrete compaction bands were reported in Bentheim sandstone by Baud et al. [6], and the episodic stress drop and the 'p-type' AE activities therein were similar to this study too. A full-fledged pattern of compaction bands is formed at $\epsilon_1 = 2.5\%$ as illustrated in Fig. 7c, where separated compaction bands are interlayered by largely undamaged zones.

Our multiscale simulations indicate the compaction bands develop from the interior of the specimens and penetrate the specimen in planar shapes. The forming pattern is rather similar to the discrete compaction bands observed in Bleurswiller sandstone with inhomogeneity in porosity [22, 23], but different than the 'compaction fronts' which form from the ends and propagate to the central part of the sample [6, 55, 57]. We also observe in our simulations of local patterns of bridge or eye structures (indicated by thick lines in Fig. 7c) which are reported in the compaction bands in Aztec sandstone [4]. They are formed due to the interactions between neighboring compaction bands.

With further increase in the axial strain, the compaction banding regions are densified and the uncompressed interlayers begin to undergo compaction. Toward the end of this stage at $\epsilon_1 = 4.5\%$ (c.f. Fig. 6), the entire specimen has been compressed to a largely homogenous state without apparent band-like pattern any more, as illustrated in Fig. 7d.

3.2 Shear-enhanced compaction bands and compactive shear bands

Closely relevant to pure compaction bands are two other deformation band patterns, shear-enhanced compaction bands and compactive shear bands. It is instructive to examine the similarities and differences among the three

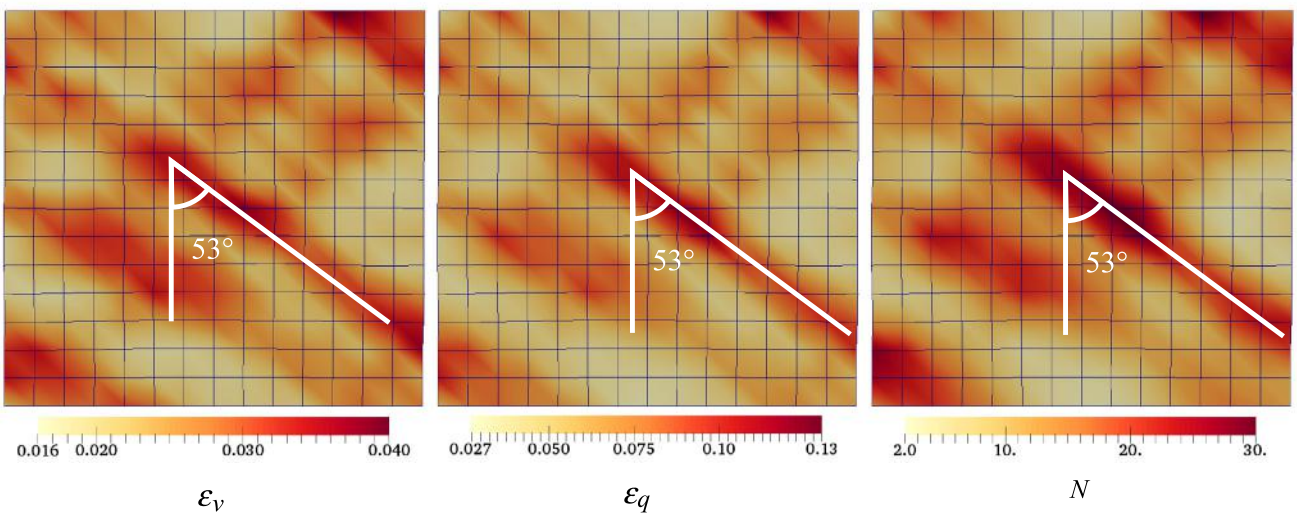

Fig. 8 Contours of ϵ_v, ϵ_q and N for the specimen under $\sigma_3 = 1$ MPa at $\epsilon_1 = 4.2\%$ showing shear-enhanced compaction bands (Case II in Table 2)

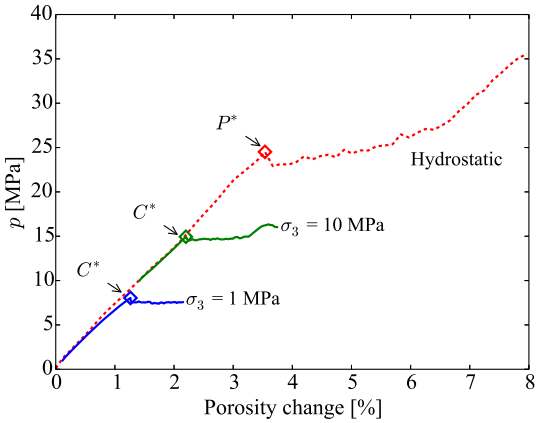

Fig. 9 Variation of mean effective pressure with porosity change during the loading (where the critical stress C^* and the critical pressure P^* signify the characteristic change in the changes in the figure when a specimen is subjected to shear and isotropic compression, respectively)

patterns as well as key contributing factors to their occurrences. A detailed cross-scale analysis of their microscopic characteristics will be presented in Sect. 4.1.

3.2.1 *Shear-enhanced compaction bands: the role of confining pressure*

Laboratory tests show that compaction bands are formed in the brittle–ductile stress transition state [40, 72]. It is well known that the confining pressure influences greatly the global stress–strain responses of a pressure-sensitive material such as sandstone, e.g., a lower confining pressure will result in a relatively brittle behavior, while a higher one leads to more ductile responses. Here we examine the role of confining pressure on the behavior of the sandstone samples by considering an additional case with a lower confining pressure (Case II in Table 2). The RVE packing is generated by isotropically unloading the previous one treated in Sect. 3.1 from $\sigma_1 = \sigma_3 = 10$MPa to $\sigma_1 = \sigma_3 = 1$ MPa. The fabric structure (interparticle contact network) of the RVE remains largely unchanged due to the applied cementation. The unloading process results in a slight increase in the initial porosity to 0.393.

The macro-sample is then subjected to biaxial compression under the lower confining pressure $\sigma_3 = 1$ MPa.

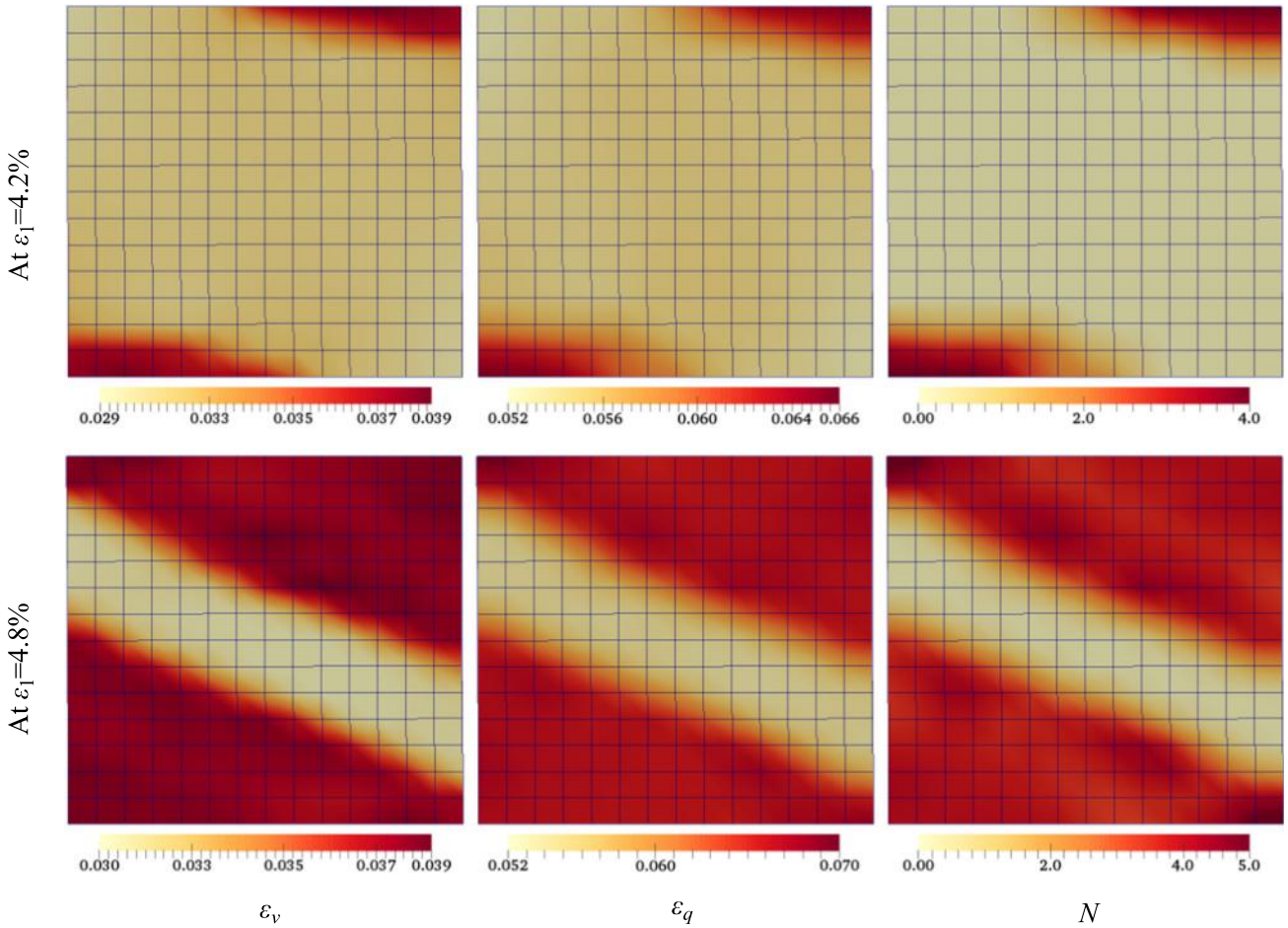

Fig. 10 Contours of ϵ_v, ϵ_q and N for the homogeneous specimen at $\epsilon_1 = 4.2\%$ and $\epsilon_1 = 4.8\%$ showing the development of compaction fronts (Case III in Table 2)

Table 2 Summary of cases and RVE types for the following multiscale modeling

Case no.	σ_3 (MPa)	Initial properties for characteristic RVE					Specimen heterogeneity in terms of C_n & C_t	Observed deformation band[b]
		RVE type	C_n, C_t (GPa)	Porosity	Particle number	Contact number		
I[a]	10	A	5	0.380	693	1140	Normal distribution, $c_v = 0.05$	Discrete CB
II	1		5	0.393		1141	Normal distribution, $c_v = 0.05$	SCB
III	10		9	0.380		1140	Homogeneous	Compaction front
IV[a]	1		5	0.393		1141	Nearly homogenous with two weak points ($C_n = C_t = 4.5$ GPa)	Cross-shaped double bands, CSB and SCB
V	2		5	0.392		1141		Cross-shaped double bands, CSB and SCB
VI	5		5	0.387		1140		Cross-shaped double bands, CSB and SCB
VII	7.5		5	0.384		1140		SCB
VIII	10		5	0.380		1140		Single CB
IX	15		5	0.372		1152		Cross-shaped double bands, CB
X	20		5	0.365		1165		Single CB
XI[a]	10	B	5	0.273	729	1231	Homogeneous	CSB
XII	10		5	0.273		1231	Nearly homogenous with two weak points ($C_n = C_t = 4.5$ GPa)	CSB
XIII	100		5	0.226		1359		CB, vanishing rapidly

[a] Cross-scale analyses of the case is discussed in Sect. 4.1

[b] The observed band patterns in our simulations will be discussed in Sect. 3, where CB stands for compaction band, SCB stands for shear-enhanced compaction band, and CSB stands for compactive shear band

The contours of ϵ_v, ϵ_q and N during the biaxial loading are illustrated in Fig. 8. A clearly different deformation pattern from that in the high confining pressure case (Case I) is observed. This type of deformation bands is named as shear-enhanced compaction bands according to some studies, as the bands are not aligned perpendicular to the major principal stress direction but form an angle of around 53° with it. Shear-enhanced compaction bands can be observed in both laboratory tests and the field, under low confining pressures when the materials behavior is brittle-dominant [12, 25, 65].

To investigate the critical pressure P^* for the onset of pore collapse, hydrostatic (isotropic) compression has been conducted on the heterogeneous specimen with a RVE of type A. The evolution of the mean effective pressure with the porosity change during the loading is illustrated in Fig. 9. The data from the previous two biaxial compression tests under $\sigma_3 = 1$ MPa and 10 MPa are also presented for comparison. As seen from the figure, the critical pressure P^* of the specimen is around 24.5 MPa, which corresponds to a maximum overburden depth of around 2 km. Note the estimated P^* for Navajo Sandstones containing pure compaction bands is 22–25 MPa based on geological observations [62]. For the biaxial compression tests, the confining pressure σ_3 should not exceed this limit. Otherwise, the oversized pores would collapse before any shearing can be applied, resulting in a cataclastic failure mode without showing clear localization patterns. For the two biaxial compression tests shown in Fig. 9, their initial responses coincide with the hydrostatic test line, indicating the porosity changes are mainly attributable to the hydrostatic compression. After a critical stress state denoted by C^* in both biaxial cases, the porosity change increases significantly. This bifurcation point C^* is commonly identified as the initiation state of accelerated porosity reduction [72, 73].

3.2.2 *Compaction fronts: the role of heterogeneity*

Another major discrepancy between the field and the laboratory observations of compaction bands is their distribution patterns. The bands in the field are clearly separated from each other by less-compressed host rock [25, 62]. However, the compaction bands are usually characterized by compaction fronts which initiate from the two ends of the specimen to its middle in laboratory tests [6, 40]. Indeed, some limited cases of interlayered compaction bands observed in the laboratory may provide clues to resolve the issue. For example, Fortin et al. [22, 23] had reported discrete compaction bands separated by largely undamaged areas in heterogeneous specimens in terms of porosity. These heterogeneities are believed to be

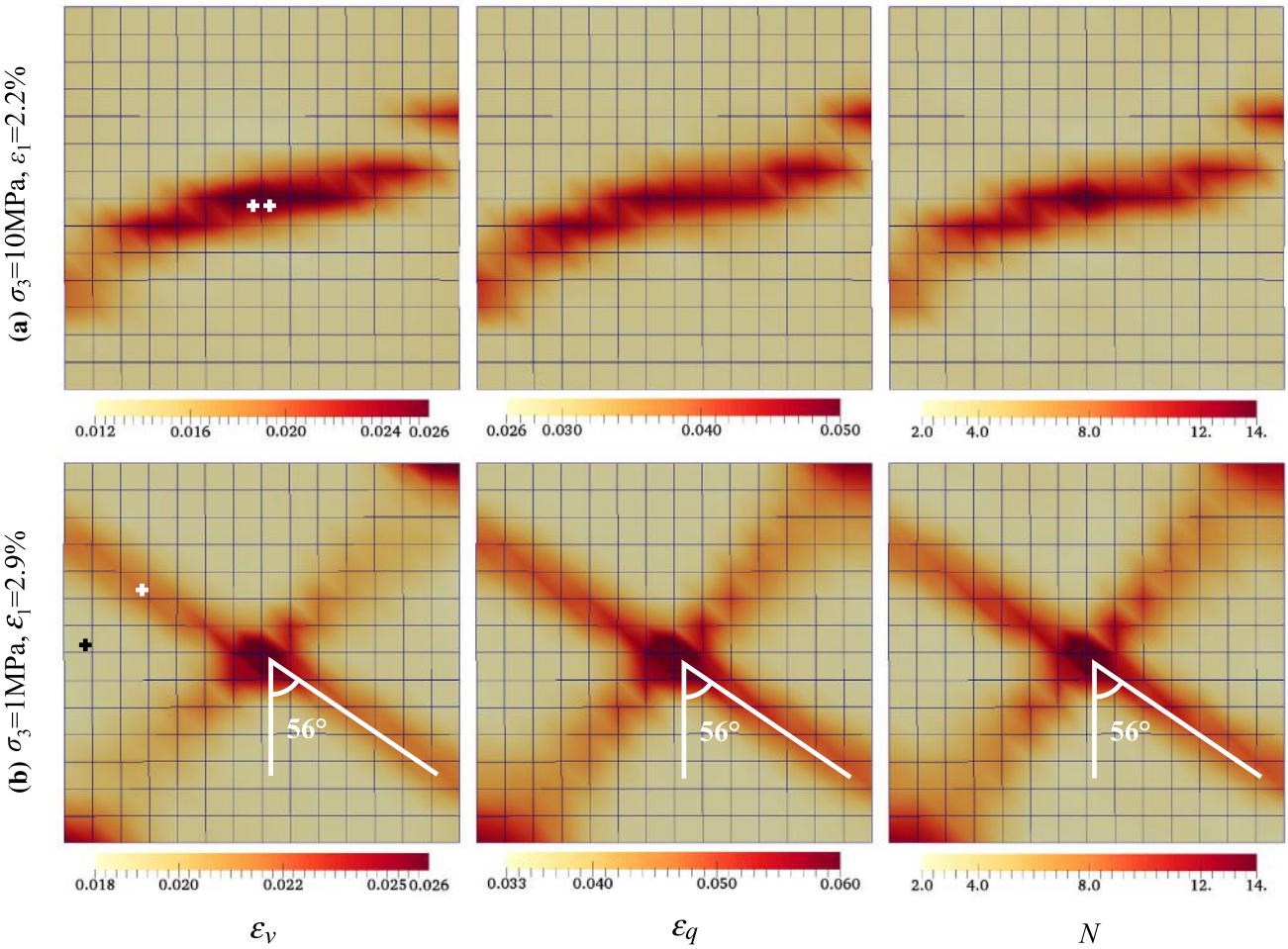

Fig. 11 Contours of ϵ_v, ϵ_q and N of the specimen with only two weak points [marked in (**a**), *left*] under **a** $\sigma_3 = 10$ MPa (Case VIII) and **b** $\sigma_3 = 1$ MPa (Case IV) showing different patterns of deformation bands

responsible for compaction bands to nucleate at some highly porous regions. In the current study, the heterogeneity introduced in local cohesion strength plays a similar role as in Fortin et al. [22] for the compaction bands to nucleate at local weak points. To verify the hypothesis, a homogeneous specimen with $C_n = C_t = 9$ GPa is tested under a confining pressure of $\sigma_3 = 10$ MPa (Case III in Table 2). Figure 10 presents the initiation and development of compaction bands in the specimen at two axial strain levels. Indeed, the compaction fronts are observed starting from the two ends of the specimen. However, unlike those reported perpendicular to the major principal stress direction [6, 40], the observed compaction fronts in our simulations are slightly tilted. This may be due to the material non-coaxiality of the RVE packing [76]. Nevertheless, similar inclined compaction fronts have also been reported in some laboratory triaxial tests [66]. Comparing the discrete compaction bands in Fig. 7 with the compaction fronts in Fig. 10, it is concluded that a homogeneous specimen is more likely to develop compaction fronts due

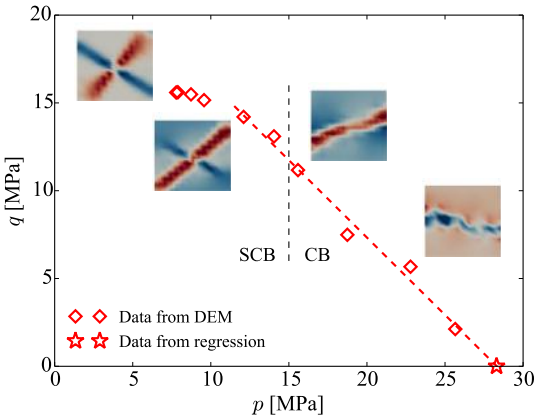

Fig. 12 Yield stresses obtained from pure DEM simulation of biaxial compression on the RVE packing (type A). Failure patterns (shown by average particle rotation $\bar{\theta}$) for specimens with two weak points under different confining pressures are shown in comparison, from *left* to *right*, for 1 MPa (Case IV), 5 MPa (Case VI), 10 MPa (Case VIII) and 20 MPa (Case X), respectively. Note that the *dashed vertical line* illustrating a rough boundary between shear-enhanced compaction band and (pure) compaction band is based on estimation without quantitative verification

partially to the boundary effects, whereas a heterogeneous specimen can develop discrete compaction bands, which nucleate from the weak points. The latter is closer to the observations in the field [25, 62] as the heterogeneity is inherent in nature.

3.2.3 *Joint influence of heterogeneities and confining pressure*

To understand the joint effects of heterogeneities (weak points) and confining pressures on the formation of deformation bands, a nearly uniform specimen ($C_n = C_t = 5$ GPa) with only two weak points ($C_n = C_t = 4.5$ GPa) embedded at the center of the domain is subjected to biaxial compression tests under two confining pressure levels $\sigma_3 = 1$ &10 MPa (Cases IV and VIII in Table 2). As seen in Fig. 11, the weak points serve as the nucleation position for the initiation of localization bands, but their subsequent developments and final patterns depend on the confining pressure levels. Under $\sigma_3 = 10$ MPa, a single compaction band spreading across the specimen horizontally (with rather mild tilting) is observed (Fig. 11a). Under $\sigma_3 = 1$ MPa, it is interesting to observe a pattern of cross-shaped double bands. One of them crosses the diagonal of the specimen and is a compactive shear band. The other tilts at an angle of 56° with respect to the major principal stress direction and is a shear-enhanced compaction band (Fig. 11b). The compactive shear band and the shear-enhanced compaction band are similar to those presented in Figs. 14 and 8, respectively. It is evident that local weak points promote the nucleation of deformation bands but are indecisive of their final patterns, while a high confining pressure facilitates the formation of compaction bands where the material shows a more ductile behavior.

We have further examined the yield stresses obtained from pure DEM simulations of the RVE packing (type A) under various confining pressures and plot the results in the

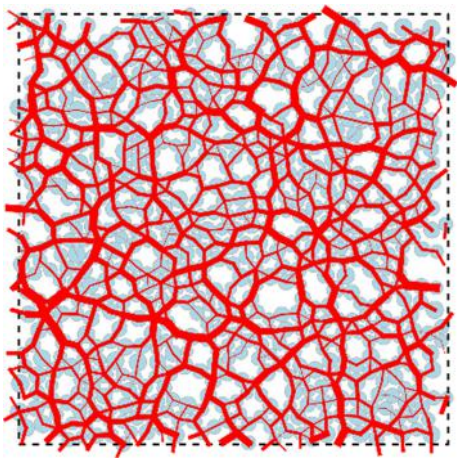

Fig. 13 Initial packing structure of a dense RVE packing (type B)

p–q plane in Fig. 12. Wong et al. [72] suggested using the following elliptical curve to describe the envelop of the stress state C^* of various sandstones:

$$\frac{(p/P^* - \gamma)^2}{(1-\gamma)^2} + \frac{(q/P^*)^2}{\delta^2} = 1$$

where γ and δ are two material constants. Fortin et al. [22] adopted an 'n power model,' $(p/a)^n + (q/b)^n = 1$, for Bleurswiller sandstone and recommended a value of n in the range of 1–1.2. It is evident that when $n = 1$, the 'n power model' can be simplified to a linear model. Our results can be well fit by a linear regression as shown in Fig. 12 with a critical pressure $P^* = 28.3$ MPa. Notice that the value of P^* herein for the RVE is different from that obtained in Sect. 3.2.1 for the specimen with heterogeneity.

The failure patterns for specimens with two weak points ($C_n = C_t = 4.5$ GPa) under 1 MPa (Case IV), 5 MPa (Case VI), 10 MPa (Case VIII) and 20 MPa (Case X), respectively, are further plotted in Fig. 12 to demonstrate the effect of confining pressure. Table 3 summarizes the

Table 3 Summary of titling angles of localization bands (counterclockwise taken as positive)

Case no.	Confining pressure (MPa)	C^* (MPa)	Band I		Band II	
			Angle to horizontal (°)	Angle to σ_1 (°)	Angle to horizontal (°)	Angle to σ_1 (°)
IV	1	8.7	−32	58	49	−41
V	2	9.6	−29	61	42	−48
VI	5	12.1	−30	60	40	−50
VII	7.5	14.0	–	–	34	−56
VIII	10	15.6	–	–	14	−76
IX	15	18.7	−26	64	21	−69
X	20	22.8	−12	78	–	–

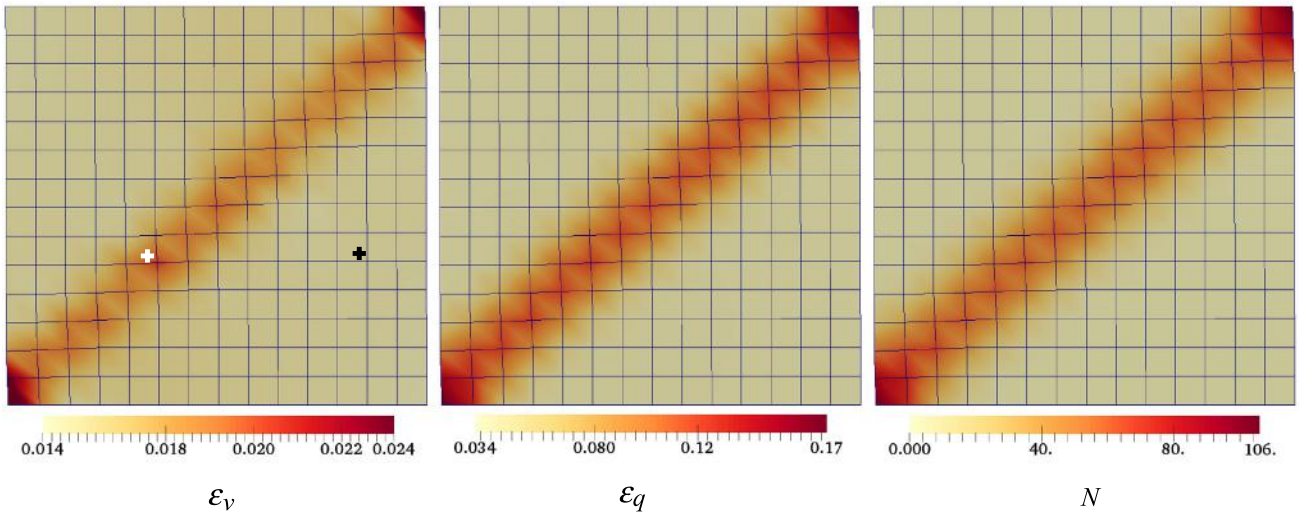

Fig. 14 Contours of ϵ_v, ϵ_q and N of the dense specimen (Case XI) at $\epsilon_1 = 3.4\%$

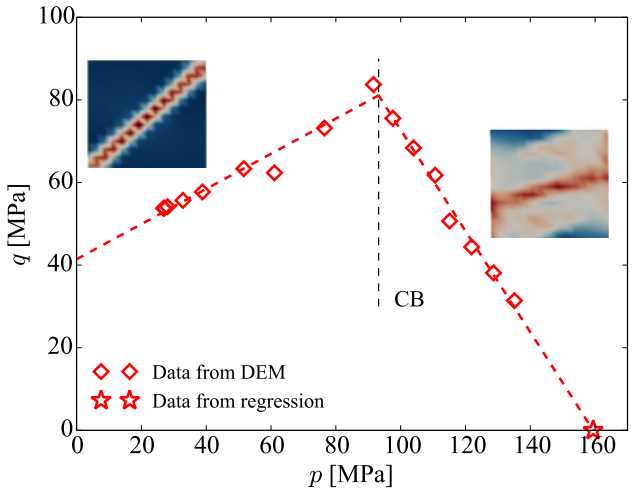

Fig. 15 Yield stresses of the dense RVE (type B) from DEM simulation. The failure patterns (in terms of $\bar{\theta}$) for specimens with two weak points under confining pressures of 10 MPa (*left*, Case XII) and 100 MPa (*right*, Case XIII) are shown for illustration

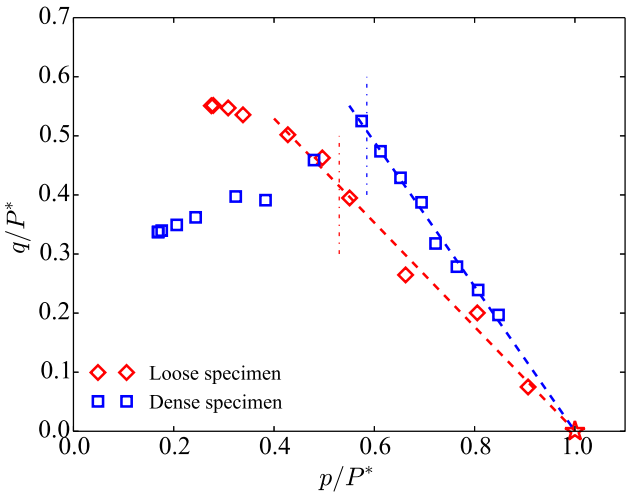

Fig. 16 Normalized yield stresses combining data in Figs. 12 and 15

variations of the tilting angle for the localized band under different confining pressures. Evidently, the tilting angles (with respect to the horizontal direction) of the localization bands decrease as the confining pressures increase. For $\sigma_3 > 10$ MPa and $C^* > 15$ MPa (please refer to Fig. 9 for the definition of C^*), the failure pattern gradually transits into low-angle compaction bands with mild tilting. The trend of tilting angle agrees rather well with the results of porous Vosges sandstone [8].

3.2.4 Compactive shear bands: the role of porosity

Shear bands are by far the most widely observed deformation band pattern in both laboratory tests and in the field [5]. Geological evidence indicates that the formation of shear bands occurs later than that of compaction bands and shear-enhanced compaction bands [21, 25]. When (shear-enhanced) compaction bands are fully developed, the overall porosity of sandstone decreases so significantly (see Fig. 7d) that shear banding may occur. We use a relatively dense RVE packing (type B in Table 2) with 729 particles and an initial porosity of 0.273 under $\sigma_3 = 10$ MPa, as illustrated in Fig. 13, to verify this. The bond cohesion strength of the RVE is set to $C_n = C_t = 5$ GPa. The specimen is prepared initially homogeneous before subjected to biaxial compression under $\sigma_3 = 10$ MPa (Case XI). The deformation pattern for this specimen at $\epsilon_1 = 3.4\%$ is illustrated in Fig. 14. A clear shear band is observed across the diagonal of the specimen wherein volumetric contraction prevails—a deformation band pattern coined by some as compactive shear band. The angle of the compactive shear band is 45° with respect to the

major principal stress direction, which is smaller than that of the shear-enhanced compaction band (53° in Fig. 8). The shear band angle should be even smaller if a sample with larger aspect ratio is used, as the square size of the specimen used in our simulation may impose a relatively strong boundary constraint on the shear band development. Another remarkable difference is that much more intense concentrations of ϵ_q and N are observed in the compactive shear band than in the (shear-enhanced) compaction bands at a comparable global axial strain level, indicative of significant shear-induced debonding.

Yield stresses derived from pure DEM simulations of this RVE (type B) are shown in p–q space in Fig. 15. The envelope could be roughly described by two straight lines bounded by a transit pressure of $p = 93.2$ MPa. The left-hand side line represents a brittle regime of the sandstone, while the right-hand side line with a negative slope denotes a plastic, compactive regime from which the critical pressure P^* is estimated as 159.4 MPa (intersection with the horizontal axis). The failure patterns for two specimens with two weak points ($C_n = C_t = 4.5$ GPa) under 10 MPa (Case XII) and 100 MPa (Case XIII) are illustrated in Fig. 15 for illustration. Interestingly, the 100 MPa case demonstrates the possible formation of compaction bands in a dense RVE under high confining pressure. However, the low porosity and high confinement apparently restrict further development of the compaction bands. The initial compaction band vanishes rapidly (from $\epsilon_1 = 2.0\%$ to $\epsilon_1 = 2.5\%$), and thereafter, the failure pattern is dominated by shear band.

We further combine the results for both the loose and the dense RVE cases in Figs. 12 and 15 using normalized stresses by their respective critical pressure and plot them in Fig. 16. The thresholds of p/P^*, shown as vertical dashed lines in the figure, correspond to the two lines in Figs. 12 and 15. We observe a threshold of 0.53 for the loose specimen and 0.58 for the dense one. The steeper slope of the regressed line for the dense specimen implies that it needs a higher q/P^* to develop compaction bands under the same p/P^* with the loose specimen. Since the dense RVE has a relatively more stable structure, a higher deviatoric stress is naturally expected to cause a compaction failure. The macro-pores in the loose specimen are more vulnerable to collapse and cause compaction failure.

4 Cross-scale analyses and discussion

4.1 Microstructural characteristics of different deformation bands

Among the unanswered questions on compaction bands, Holcomb et al. [34] mentioned the unclear role of microstructural attributes in the formation and development of deformation bands. The differences in microscopic properties among compaction bands, shear-enhanced compaction bands and compactive shear bands are of great importance to understand their physical mechanisms. Eichhubl et al. [21] observed these different deformation bands formed in the field with scanning-electron microscope images. Charalampidou et al. [11, 12] investigated the microscopic characteristics of these different deformation bands

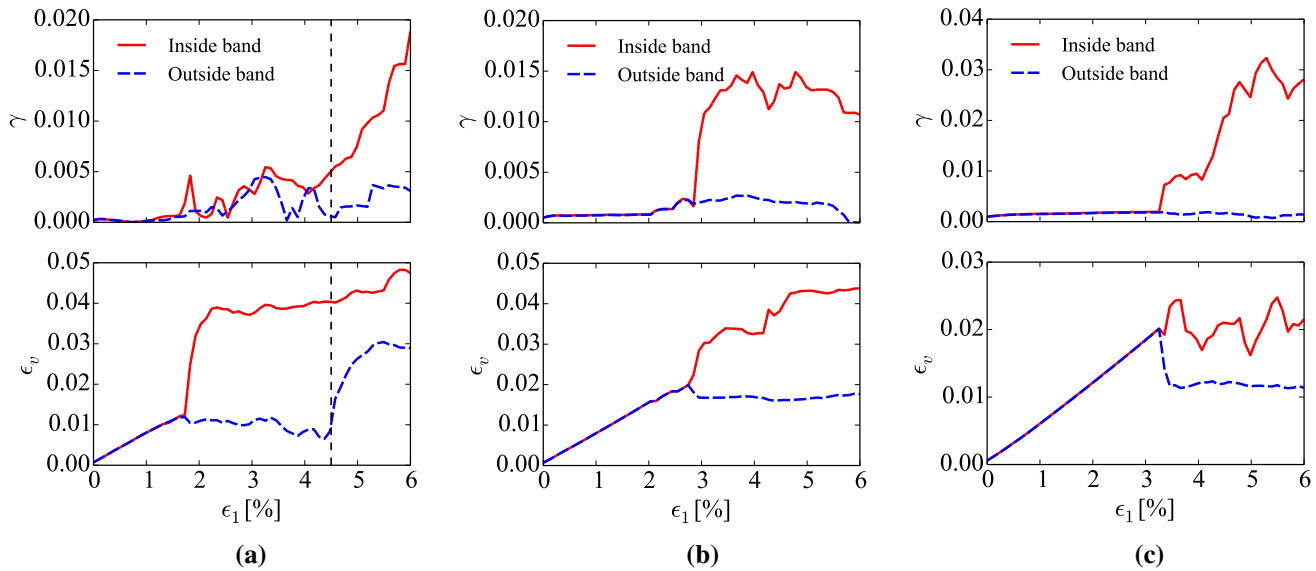

Fig. 17 Comparison of different deformation bands in terms of γ and ϵ_v: **a** compaction band (Case I), **b** shear-enhanced compaction band (Case IV), **c** compactive shear band (Case XI). The *vertical dashed line* in **a** indicates the transition state from stage II to stage III (Fig. 6)

developed in their experiments using means of AE, ultrasonic tomography and X-ray tomography. They further concluded that shear-enhanced compaction bands are more similar to compaction bands than to compactive shear bands. The multiscale approach provides a convenient pathway to bridge the macroscopic observations with the microscopic characteristics, as will be demonstrated below.

4.1.1 Volumetric strain versus shear strain

The shear strain, measured by $\gamma = 2|\epsilon_{13}|$ and comparable to the so-called shear offset by some, is widely adopted to distinguish different types of deformation bands in the field [24, 49]. Compaction band is typically characterized by a small shear offset [49], while according to Eichhubl et al. [21], the shear offset in shear-enhanced compaction bands

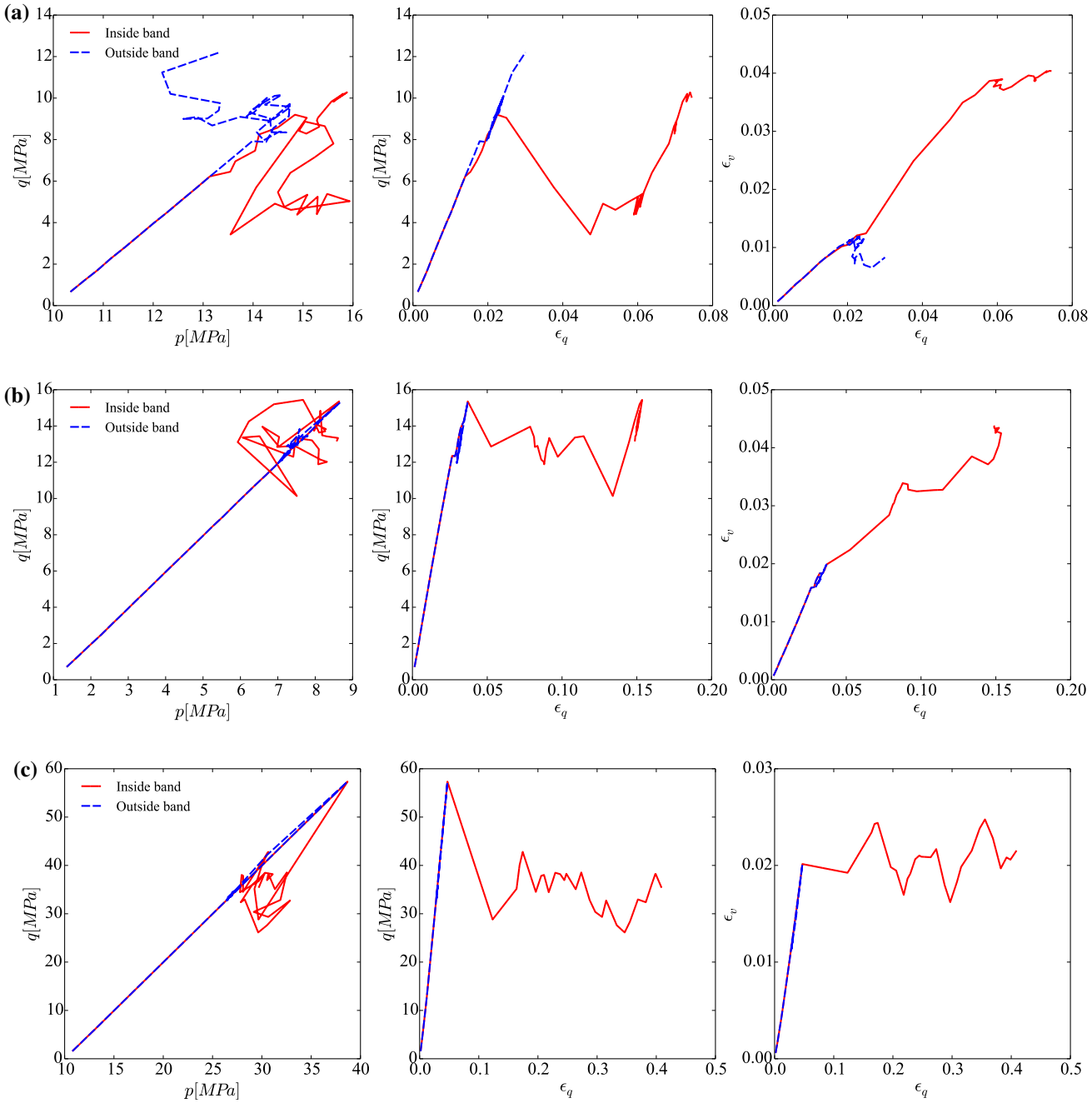

Fig. 18 The local material responses extracted from RVE for the points inside and outside the deformation band. **a** Compaction band (Case I, ϵ_1 up to 4.5%), **b** shear-enhanced compaction band (Case IV), **c** compactive shear band (Case XI)

is around 1/10 of the band thickness (i.e., $\gamma \approx 0.1$) and it is much larger for compactive shear bands in the field. We select two Gauss points, one inside (marked by white cross) and one outside (marked by black cross) of the band, as indicated in Figs. 7, 11 and in Fig. 14 for the different deformation bands, to compare the evolutions of γ and ϵ_v. The results are presented in Fig. 17, showing the following observations:

(1) In the case of compaction band formed in an initially heterogeneous specimen under $\sigma_3 = 10$ MPa, γ for both points (marked in Fig. 7c, middle) remains negligibly small (<0.005) before entering stage III shown in Fig. 6. ϵ_v inside the band increases dramatically when the specimen enters stage II (Fig. 6), whereas ϵ_v outside the band remains largely constant.
(2) For the shear-enhanced compaction band developed in the nearly homogeneous specimen with two weak points (marked in Fig. 11b, left) under $\sigma_3 = 1$ MPa, γ inside the band increases to a relatively large value around 0.015. The responses for γ outside the band and ϵ_v at both points are similar to those in the compaction band case.
(3) For the case of compactive shear band developed in the initially homogeneous specimen with a low porosity (chosen points marked in Fig. 14 left), the magnitude of γ inside the band increases remarkably to about 0.03. Meanwhile, ϵ_v at the two points are smaller than that in the previous two cases.

In summary, the compaction bands are characterized by small shear strain but relatively large volumetric strain, whereas the compactive shear bands exhibit large shear strain but relatively small volumetric strain. The shear strain is moderate in the shear-enhanced compaction band as an intermediate case between the other two.

4.1.2 Comparison of the local responses

The hierarchical multiscale approach offers direct linking of the macro-observations with their local material responses and underlying microstructural mechanisms at the RVE level. To demonstrate this, we present in Fig. 18 the stress path in the p–q space, the evolution of q and ϵ_v with ϵ_q at the two selected Gauss points (one inside and one outside band) for the three different deformation bands as discussed in Sect. 4.1.1, from which the following observations are made:

(1) Prior to the inception of localization, the local responses at both selected points are almost identical in all three cases, showing an almost linear, elastic behavior. When deformation bands occur, the stress paths become rather complicated in all cases.
(2) When pure compaction bands occur (Fig. 18a), it is interesting to observe that the material point outside the band shows a decrease in p but an increase in q (with apparent fluctuations) and a dilative behavior (decrease in ϵ_v) with increased ϵ_q, a phenomenon not found in other deformation band cases. For the point inside the band, both p and q undergo a first decrease before increase. Meanwhile, the post-bifurcation compaction is accelerated in the sample, manifested by an increasing slope of ϵ_v in ϵ_v–ϵ_q diagram than the elastic stage, due largely to the collapse of pores.
(3) The point outside the band for both cases of shear-enhanced compaction band and compactive shear band depicts a nearly elastic unloading process after localization occurs.
(4) For the point inside the shear-enhanced compaction band, both p and q decrease slightly with some fluctuations in the post-bifurcation state, and the compaction of the sample slows down as compared to the elastic stage, with a slightly decreased slope of ϵ_v in ϵ_v–ϵ_q diagram. As for the compactive shear band case, both p and q for the point inside the band drop dramatically before become steady with certain fluctuations during the post-bifurcation stage. The overall density of the specimen becomes steady too (albeit with fluctuations).

4.1.3 Fabric anisotropy and pore collapse

Fabric has been frequently used to characterize the microstructural attributes in a granular material. We employ the widely accepted contact normal-based fabric tensor defined by Oda [52]. As the interparticle cohesion allows a contact to sustain both compressive and tensile forces, these two types of contacts are treated separately

$$\boldsymbol{\phi}^{\blacksquare} = \int_{\Theta} E(\Theta)\mathbf{n}_c^{\blacksquare} \otimes \mathbf{n}_c^{\blacksquare} \mathrm{d}\Theta = \frac{1}{N_c^{\blacksquare}} \sum_{N_c^{\blacksquare}} \mathbf{n}_c^{\blacksquare} \otimes \mathbf{n}_c^{\blacksquare} \tag{7}$$

where the superscript '$\blacksquare$' denotes c for compressive contact or t for tensile contact. $N_c^{\blacksquare}$ is the number of compressive or tensile contacts within the packing. $\mathbf{n}_c^{\blacksquare}$ is the unit vector in the outward normal direction of a contact. Θ is the orientation of $\mathbf{n}_c^{\blacksquare}$ in the global coordinate system. '$\otimes$' denotes the dyadic operator between two vectors. The distribution function $E(\Theta)$ can be approximated by a second-order Fourier expansion:

$$E(\Theta) = \frac{1}{2\pi}\left[1 + \mathbf{F}_a^{\blacksquare} : \left(\mathbf{n}_c^{\blacksquare} \otimes \mathbf{n}_c^{\blacksquare}\right)\right] \tag{8}$$

where the deviatoric tensor $\mathbf{F}_a^{\blacksquare}$ quantifies the fabric anisotropy

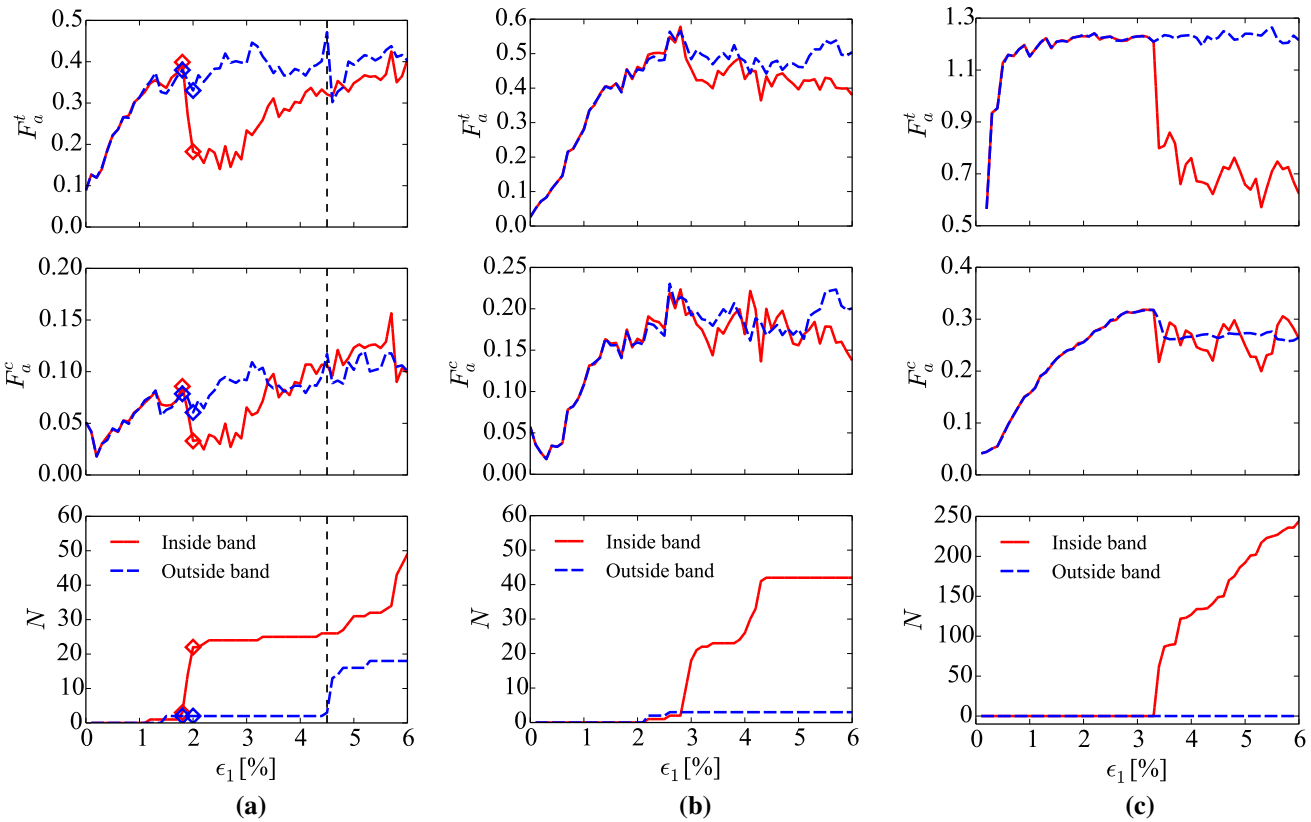

Fig. 19 Evolution of anisotropy and debonding number with ϵ_1 in different cases: **a** compaction band (Case I), **b** shear-enhanced compaction band (Case IV), **c** compactive shear band (Case XI). The *vertical dashed line* in **a** indicates the transition state from stage II to stage III (in Fig. 6)

$$\mathbf{F}_a^{\blacksquare} = 4\left(\boldsymbol{\phi}^{\blacksquare} - \frac{1}{2}\boldsymbol{\delta}\right) \tag{9}$$

where $\boldsymbol{\delta}$ is the Kronecker delta. The anisotropy intensity could be measured by

$$F_a^{\blacksquare} = \sqrt{\frac{1}{2}\mathbf{F}_a^{\blacksquare} : \mathbf{F}_a^{\blacksquare}} \tag{10}$$

The evolutions of F_a^t and F_a^c at the two selected Gauss points (one inside and one outside band) for the three different deformation bands discussed in Sect. 4.1.1 are illustrated in Fig. 19, based on which the following general observations are made:

(1) The anisotropy of compressive contacts F_a^{c} is generally much smaller than that of the tensile contacts F_a^{t} in all three cases.
(2) Among the three cases, the anisotropy intensities are the largest in the compactive shear band case and the smallest in the pure compaction band case.
(3) In all three cases, F_a^{t} at the point outside the band increases steadily with the external load to a relatively steady (albeit with fluctuations) value, while F_a^{t} for the point inside the band reaches a peak before decreasing in both cases of shear-enhanced compaction band and compactive shear band due to significant increase in debonding of the tensile contacts within the band (bottom row of Fig. 19). Indeed, there is a sudden drop of F_a^{t} for the compactive shear band case at around 3.2% axial strain due apparently to a dramatic surge of debonding (see the debonding figure at the bottom row).
(4) Interestingly, in the pure compaction band case as shown in Fig. 19a, F_a^{t} inside the band first experiences a sharp drop and then steadily builds up its value again. The dramatic drop is due apparently to a sudden burst of debonding events within the band at an axial strain between 1.8 and 2%. The steady buildup stage of F_a^{t} is associated with a calm plateau period in debonding both inside and outside of the band between 2 and 4.4% of axial strain. During this plateau stage, no major debonding occurs, while the entire sample experience excessive volume reduction, which leads to steadily increased contacts both in compression and tension.
(5) The evolution of F_a^{c} is generally similar to F_a^{t} in the cases of compaction band and shear-enhanced compaction band. In the compactive shear band case, it is interesting to observe that both F_a^{c} and F_a^{t} outside the

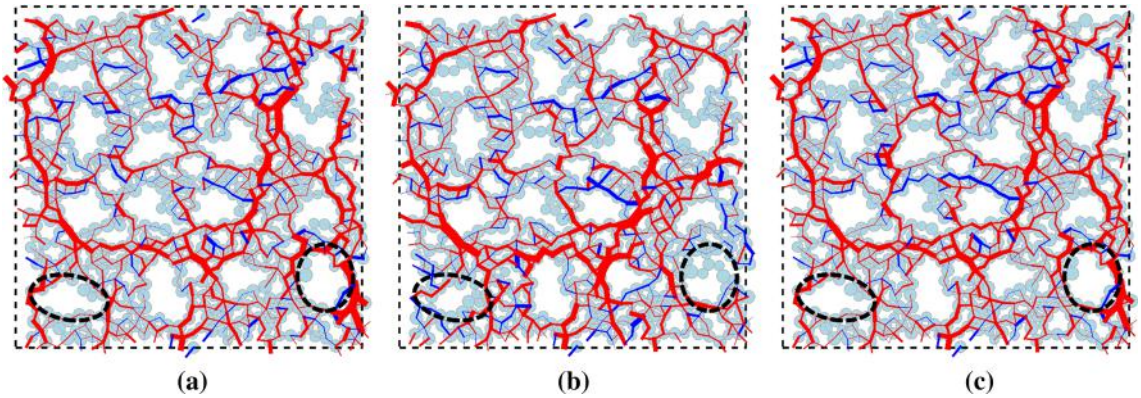

Fig. 20 RVE structure of point inside the compaction band **a** before and **b** after pore collapses and **c** the structure of the point outside the bands at $\epsilon_1 = 2.0\%$. Color interpretation: *red* for compressive contacts and *blue* for tensile contacts (color figure online)

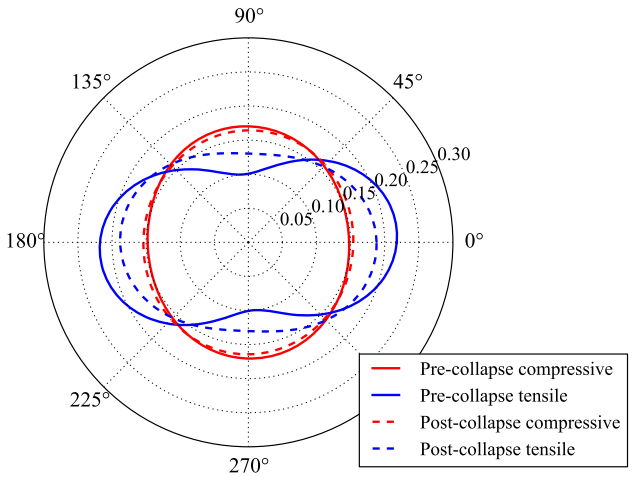

Fig. 21 Fourier approximations of the contact normal distributions for the point inside the compaction band

band experience much less fluctuations than the other two cases. The drop of F_a^c at $\epsilon_1 = 3.2\%$ is due to the unloading after the localization.

(6) For the point outside the band, the debonding number shows a surge in the pure compaction band case at around 4.5% axial strain, whereas it is negligibly small or stays almost zero for the other two cases. This is consistent with the observation in Fig. 7d that the compaction bands propagate and penetrate the whole specimen, while the other two bands are more localized within confined regions.

(7) Regarding the debonding at the point inside the band, the pure compaction band case shows a relatively long calm plateau of debonding number which is followed by the accelerating increase after 4.5% axial strain. In the case of shear-enhanced compaction band, there are two plateau stages of debonding appears, the first one being brief and the second long and sustaining. The debonding number in compactive shear band case increases drastically after 3.2% axial stain without showing any plateau stage.

To visualize the microstructural change in the local material point, a RVE packing inside the pure compaction band is selected. Its force–chain systems before and after the burst of pore collapse (at $\epsilon_1 = 1.8\,\&\,2.0\%$, marked in Fig. 19a) are plotted in Fig. 20a, b. Two spots with apparent macro-pore collapse are identified in the figure (shown as two dashed ellipsoids). For comparison, the force–chain system of the point outside the band at $\epsilon_1 = 2.0\%$ is illustrated in Fig. 20c, which shows no apparent pore collapses.

Figure 21 shows rose diagrams for the contact normal distributions for both tensile and compressive contacts. Clearly, the anisotropy of tensile contacts decreases noticeably after pore collapse, whereas its change in the compressive contacts is vanishingly small. These observations are consistent with those shown in Fig. 19a.

4.1.4 Average particle rotation

Particle rotation is another important signature characterizing different deformation bands [29, 76]. In this study, we use the average particle rotation defined by $\bar{\theta} = \sum_{N_p} \theta_p / N_p$, where N_p is the number of particles within the packing, θ_p is the accumulated rotation of individual particles. Anticlockwise rotation is treated as positive.

The contours of $\bar{\theta}$ for different types of deformation bands are illustrated in Fig. 22. The distribution of $\bar{\theta}$ in the initially heterogeneous specimen (Case I, c.f. Fig. 7c), which develops the discrete compaction bands, is relatively scattered (Fig. 22a). For the single compaction band developed in the nearly homogeneous specimen with two weak points under $\sigma_3 = 10$ MPa (Case VIII) and the shear-enhanced compaction band developed in the same specimen but under a lower confining pressure (Case IV,

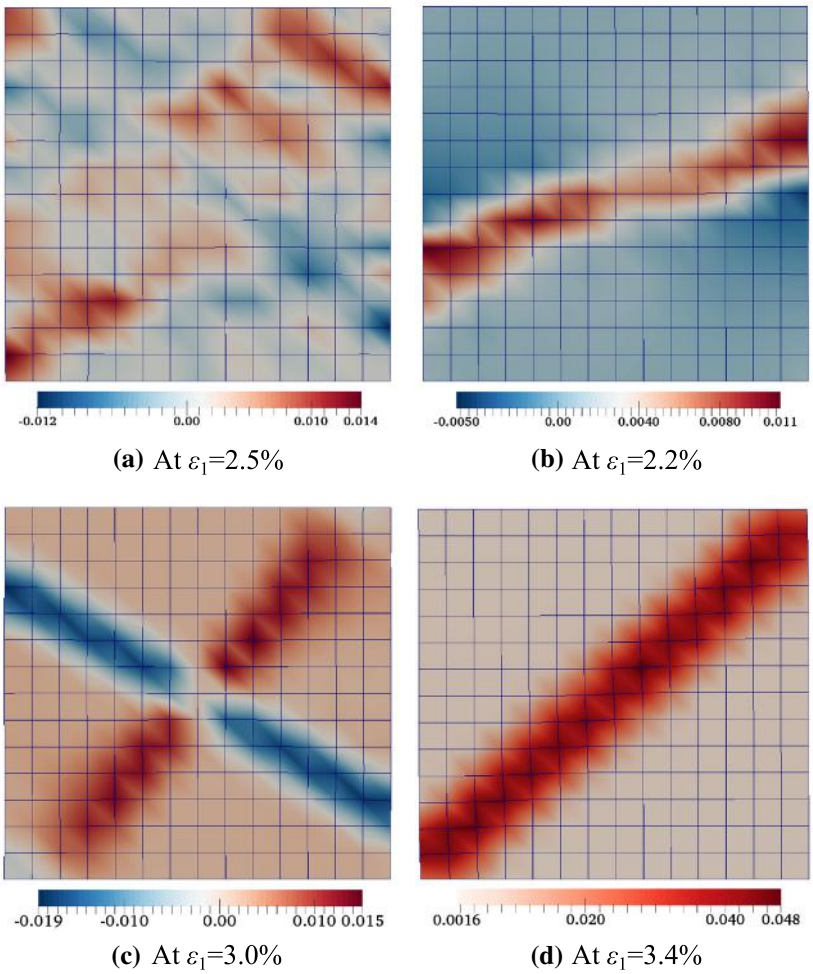

(a) At ε_1=2.5% **(b)** At ε_1=2.2%

(c) At ε_1=3.0% **(d)** At ε_1=3.4%

Fig. 22 Average particle rotation for **a** discrete compaction bands (Case I), **b** single compaction band (Case VIII), **c** shear-enhanced compaction band (Case IV) and **d** compactive shear band (Case XI)

$\sigma_3 = 1$ MPa), similar localized bands are observed from the particle rotation contours. Nevertheless, the magnitude of $\bar{\theta}$ is generally small in these cases. Zhao and Guo [76] confirmed a close correlation between the particle rotation and shear deformation in shear band in sand. Interestingly, macro-observations of compaction band may lead to misleading impression that a compaction band contains only volumetric contraction. But our multiscale results extracted from the RVE and microscale information suggest that both noticeable particle rotations (see Fig. 22) and significant shear deformation (see Figs. 7, 11, middle) occur within a compaction band. Indeed, all four indicative quantities used in our study, $\epsilon_{\mathrm{v}}, \epsilon_q, N$ and $\bar{\theta}$, as shown in these figures, collectively show intensely localized deformation patterns almost perpendicular to the direction of σ_1, a signature feature of compaction bands.

In contrast, the compactive shear band developed in the homogeneous specimen with a low porosity (Case XI) depicts much larger $\bar{\theta}$ (3–4 times larger) compared with the previous cases. From the observations shown in Figs. 17, 18, 19 and Fig. 22, it is evident that shear-enhanced compaction bands are more similar to compaction bands in terms of their microscopic characteristics, whereas compactive shear bands differ from the two distinctively. The observations are consistent with Eichhubl et al. [21] and Charalampidou et al. [11, 12].

4.2 Mesh dependency

Our multiscale FEM solutions do show certain mesh dependency when modeling the strain localization problems due to the lack of an intrinsic length scale in our local material model. This problem could possibly be solved with a nonlocal scheme (e.g., [42]), but is beyond the scope of this study. Nevertheless, to examine the influence of mesh density on the compaction bands in the multiscale approach, an additional test on the initially heterogeneous specimen ($\bar{C}_{\mathrm{n}} = \bar{C}_{\mathrm{t}} = 5\,\mathrm{GPa}, c_{\mathrm{v}} = 0.05$) under $\sigma_3 = 10$ MPa with a finer mesh (28×28 quadrilateral elements, exact the same spatial distribution of cohesion strength

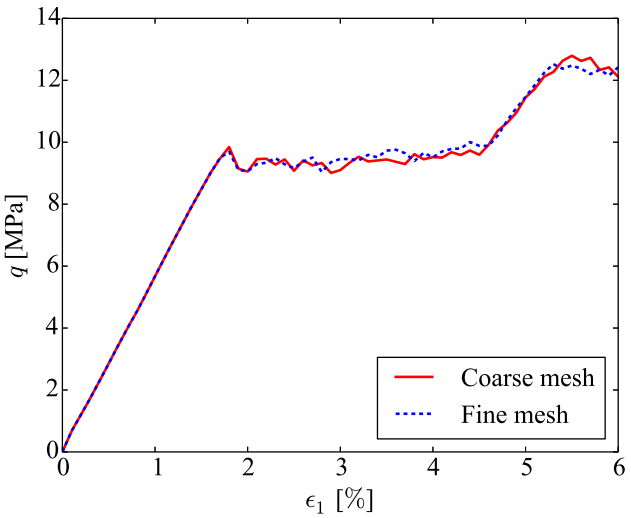

Fig. 23 Sensitivity of the stress–strain relationship to mesh density

with Case I) is conducted. The comparisons between the coarse mesh (14×14 elements, Case I) results and the current ones are shown in Figs. 23 and 24. Their global stress–strain responses depict only slight differences. By comparing Fig. 24 with Fig. 7c, the contours of ϵ_v, ϵ_q and N are also rather similar in terms of the overall patterns and the positions of the deformation bands. Hence, it is safe to conclude that the influence of mesh density is not excessively significant in the current multiscale study.

5 Conclusions

A multiscale approach has been employed to model and analyze compaction bands in high-porosity sandstones. Based on coupled FEM/DEM and without assuming phenomenological constitutive assumption of the material, the approach has been shown to successfully reproduce the onset and the development of different deformation bands in porous sandstones, including the discrete compaction bands, the compaction fronts, the shear-enhanced compaction bands and the compactive shear bands. The formation of different deformation bands depends crucially on the sample porosity, heterogeneity and applied pressure level. In the absence of particle crushing, the formation of compaction bands and shear-enhanced compaction bands is found attributable to the significant porosity reduction caused by debonding and subsequent pore collapse. The global stress–strain responses of the specimen developing compaction bands are consistent with the triaxial test results on Castlegate and Bentheim sandstones. Their debonding processes also resemble the so-called "p-type" AE activity.

High porosity and high confining pressure are identified as two major factors favoring the formation of compaction bands. While a higher confining pressure renders a sandstone more ductile, higher porosity makes it more vulnerable to pore collapse. With the decrease in confining pressure and/or the decrease in porosity, a deformation band pattern may transit from a compaction band to a shear-enhanced compaction band which may further evolve to a compactive shear band. Discrete compaction bands are found more likely to develop in heterogeneous specimens, where the local weak points may act as nuclei for the initiation of compaction bands. Compaction fronts are more likely to occur in a homogeneous specimen due partially to the boundary constraint.

Our multiscale results show that compactive shear bands commonly accompany large shear strain but small volumetric strain, whereas pure compaction bands have large

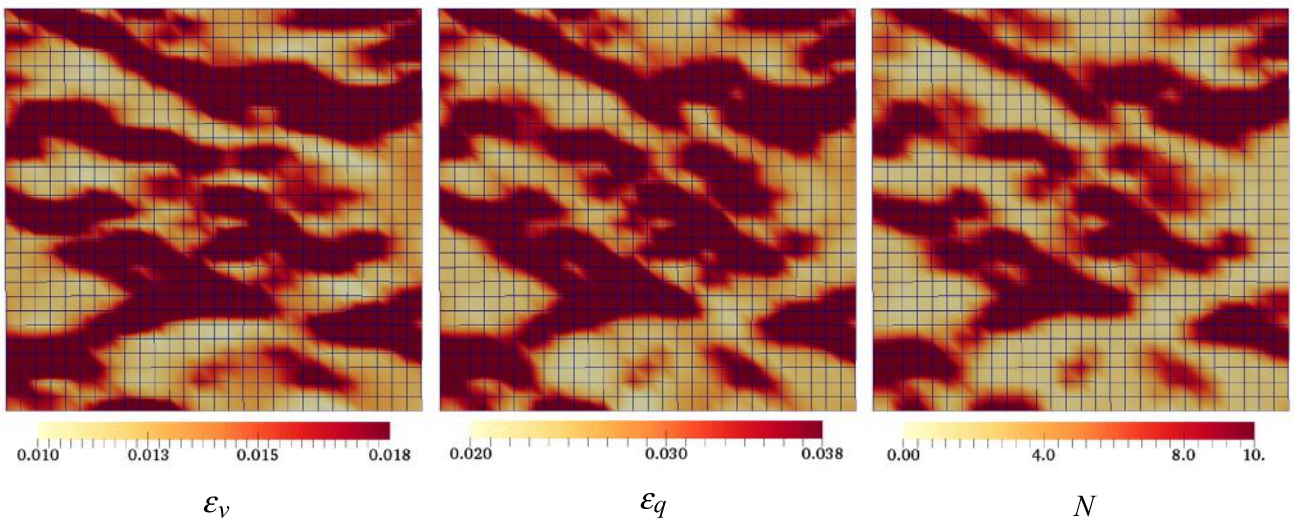

Fig. 24 Contours of ϵ_v, ϵ_q and N of the specimen with fine mesh at $\epsilon_1 = 2.5\%$

volumetric strain but little shear strain. The shear strain in the shear-enhanced compaction band is intermediate. Further cross-scale analyses indicate that the fabric anisotropies for both tensile and compressive contacts inside the shear bands are much larger than those in compaction bands and shear-enhanced compaction bands. The average particle rotation in shear bands is also the largest. These observations confirm that shear-enhanced compaction bands are more similar to pure compaction bands, whereas compactive shear bands differ essentially from either of the two compaction band patterns [11, 12, 21].

The current study can be further extended in the future for more realistic multiscale modeling of compaction bands. First, all simulations in the study have been performed in 2D scenarios, while the formation and development of compaction bands may have been caused by complicated 3D loading conditions [36]. Second, the dual-porosity structure considered in the study is oversimplified. More realistic pore/particle structures of sandstones based on experimental imaging, along with possible particle crushing, need to be carefully considered to generate realistic RVE for the multiscale modeling. Third, the heterogeneity considered in the study is fully random, whereas certain spatial correlations have been observed in the field for various material properties. Last, since the formation of compaction band is widely concerned in reservoir engineering and oil industry, a fully coupled hydro-mechanical problem needs to be considered in the presence of water/oil [30, 69] wherein the influence of pore water pressure can be examined. All these aspects will be addressed in a future study.

Acknowledgements This work was partially supported by Research Grants Council of Hong Kong through a Theme-based Research Project (No. T22-603/15N) and a Collaborative Research Fund project (Grant No. C6012-15G) and by Natural Science Foundation of China under Project No. 51679207. The authors are also grateful for Prof. Teng-fong Wong of CUHK and Dr. WaiChing Sun of Columbia University for useful discussion on this topic.

References

1. Andrade JE, Avila CF, Hall SA, Lenoir N, Viggiani G (2011) Multiscale modeling and characterization of granular matter: from grain kinematics to continuum mechanics. J Mech Phys Solids 59(2):237–250. doi:10.1016/j.jmps.2010.10.009
2. Antonellini MA, Aydin A, Pollard DD (1994) Microstructure of deformation bands in porous sandstones at Arches National Park, Utah. J Struct Geol 16(7):941–959. doi:10.1016/0191-8141(94)90077-9
3. Aydin A (1978) Small faults formed as deformation bands in sandstone. Pure Appl Geophys 116(4–5):913–930. doi:10.1007/BF00876546
4. Aydin A, Ahmadov R (2009) Bed-parallel compaction bands in aeolian sandstone: their identification, characterization and implications. Tectonophysics 479(3–4):277–284. doi:10.1016/j.tecto.2009.08.033
5. Aydin A, Borja RI, Eichhubl P (2006) Geological and mathematical framework for failure modes in granular rock. J Struct Geol 28(1):83–98. doi:10.1016/j.jsg.2005.07.008
6. Baud P, Klein E, Wong TF (2004) Compaction localization in porous sandstones: spatial evolution of damage and acoustic emission activity. J Struct Geol 26(4):603–624. doi:10.1016/j.jsg.2003.09.002
7. Bernabé Y, Fryer DT, Hayes JA (1992) The effect of cement on the strength of granular rocks. Geophys Res Lett 19(14):1511. doi:10.1029/92GL01288
8. Bésuelle P (2001) Compacting and dilating shear bands in porous rock: theoretical and experimental conditions. J Geophys Res Solid Earth 106(B7):13435–13442. doi:10.1029/2001JB900011
9. Bésuelle P, Desrues J, Raynaud S (2000) Experimental characterisation of the localisation phenomenon inside a Vosges sandstone in a triaxial cell. Int J Rock Mech Min Sci 37(8):1223–1237. doi:10.1016/S1365-1609(00)00057-5
10. Challa V, Issen KA (2004) Conditions for compaction band formation in porous rock using a two-yield surface model. J Eng Mech 130(9):1089–1097. doi:10.1061/(ASCE)0733-9399(2004)130:9(1089)
11. Charalampidou E-M, Hall SA, Stanchits S, Viggiani G, Lewis H (2014) Shear-enhanced compaction band identification at the laboratory scale using acoustic and full-field methods. Int J Rock Mech Min Sci 67:240–252. doi:10.1016/j.ijrmms.2013.05.006
12. Charalampidou EM, Hall SA, Stanchits S, Lewis H, Viggiani G (2011) Characterization of shear and compaction bands in a porous sandstone deformed under triaxial compression. Tectonophysics 503(1–2):8–17. doi:10.1016/j.tecto.2010.09.032
13. Cheng Y, Nakata Y, Bolton M (2003) Discrete element simulation of crushable soil. Géotechnique 53(7):633–641. doi:10.1680/geot.2003.53.7.633
14. Cheung CSN, Baud P, Wong TF (2012) Effect of grain size distribution on the development of compaction localization in porous sandstone. Geophys Res Lett 39(21):6–10. doi:10.1029/2012GL053739
15. Ciantia MO, Hueckel T (2013) Weathering of submerged stressed calcarenites: chemo-mechanical coupling mechanisms. Géotechnique 63(9):768–785. doi:10.1680/geot.SIP13.P.024
16. Das A, Nguyen GD, Einav I (2011) Compaction bands due to grain crushing in porous rocks: a theoretical approach based on breakage mechanics. J Geophys Res 116(B8):B08203. doi:10.1029/2011JB008265
17. Das A, Nguyen GD, Einav I (2013) The propagation of compaction bands in porous rocks based on breakage mechanics. J Geophys Res Solid Earth 118(5):2049–2066. doi:10.1002/jgrb.50193
18. Dattola G, di Prisco C, Redaelli I, Utili S (2014) A distinct element method numerical investigation of compaction processes in highly porous cemented granular materials. Int J Numer Anal Methods Geomech 38(11):1101–1130. doi:10.1002/nag.2241
19. Delenne JY, El Youssoufi MS, Cherblanc F, Bénet JC (2004) Mechanical behaviour and failure of cohesive granular materials. Int J Numer Anal Methods Geomech 28(15):1577–1594. doi:10.1002/nag.401
20. Eichhubl P, Taylor WL, Pollard DD, Aydin A (2004) Paleo-fluid flow and deformation in the Aztec Sandstone at the Valley of Fire, Nevada—evidence for the coupling of hydrogeologic, diagenetic, and tectonic processes. Geol Soc Am Bull 116(9):1120. doi:10.1130/B25446.1
21. Eichhubl P, Hooker JN, Laubach SE (2010) Pure and shear-enhanced compaction bands in Aztec Sandstone. J Struct Geol 32(12):1873–1886. doi:10.1016/j.jsg.2010.02.004

22. Fortin J, Stanchits S, Dresen G, Guéguen Y (2006) Acoustic emission and velocities associated with the formation of compaction bands in sandstone. J Geophys Res 111(B10):B10203. doi:10.1029/2005JB003854
23. Fortin J, Stanchits S, Dresen G, Gueguen Y (2009) Acoustic emissions monitoring during inelastic deformation of porous sandstone: comparison of three modes of deformation. Pure Appl Geophys 166(5–7):823–841. doi:10.1007/s00024-009-0479-0
24. Fossen H, Schultz RA, Shipton ZK, Mair K (2007) Deformation bands in sandstone: a review. J Geol Soc Lond 164(4):1–15. doi:10.1144/0016-76492006-036
25. Fossen H, Schultz RA, Torabi A (2011) Conditions and implications for compaction band formation in the Navajo Sandstone, Utah. J Struct Geol 33(10):1477–1490. doi:10.1016/j.jsg.2011.08.001
26. Gao Z, Zhao J (2013) Strain localization and fabric evolution in sand. Int J Solids Struct 50(22–23):3634–3648. doi:10.1016/j.ijsolstr.2013.07.005
27. Guo N, Zhao J (2014) A coupled FEM/DEM approach for hierarchical multiscale modelling of granular media. Int J Numer Methods Eng 99(11):789–818. doi:10.1002/nme.4702
28. Guo N, Zhao J (2016) 3D multiscale modeling of strain localization in granular media. Comput Geotech 80:360–372. doi:10.1016/j.compgeo.2016.01.020
29. Guo N, Zhao J (2016) Multiscale insights into classical geomechanics problems. Int J Numer Anal Methods Geomech 40(3):367–390. doi:10.1002/nag.2406
30. Guo N, Zhao J (2016) Parallel hierarchical multiscale modelling of hydro-mechanical problems for saturated granular soils. Comput Methods Appl Mech Eng 305:37–61. doi:10.1016/j.cma.2016.03.004
31. Guo N, Zhao J, Sun WC (2016) Multiscale analysis of shear failure of thick-walled hollow cylinder in dry sand. Géotech Lett 6(1):77–82. doi:10.1680/jgele.15.00149
32. Hazzard JF, Young RP, Maxwell SC (2000) Micromechanical modeling of cracking and failure in brittle rocks. J Geophys Res 105:16683–16697. doi:10.1029/2000JB900085
33. Hill RE (1989) Analysis of deformation bands in the Aztec Sandstone. University of Nevada, Reno
34. Holcomb D, Rudnicki JW, Issen KA, Sternlof K (2007) Compaction localization in the Earth and the laboratory: state of the research and research directions. Acta Geotech 2(1):1–15. doi:10.1007/s11440-007-0027-y
35. Holcomb DJ, Olsson WA (2003) Compaction localization and fluid flow. J Geophys Res 108(B6):2290–2302. doi:10.1029/2001JB000813
36. Issen KA, Rudnicki JW (2000) Conditions for compaction bands in porous rock. J Geophys Res 105(B9):21529–21536. doi:10.1029/2000JB900185
37. Katsman R, Aharonov E (2006) A study of compaction bands originating from cracks, notches, and compacted defects. J Struct Geol 28(3):508–518. doi:10.1016/j.jsg.2005.12.007
38. Katsman R, Aharonov E, Haimson BC (2009) Compaction bands induced by borehole drilling. Acta Geotech 4(3):151–162. doi:10.1007/s11440-009-0086-3
39. Kim SY, Sasaki Y (2013) Simulation of crack formation in an anisotropic coke using discrete element method. Fuel 106:357–364. doi:10.1016/j.fuel.2012.10.070
40. Klein E, Baud P, Reuschlé T, Wong TF (2001) Mechanical behaviour and failure mode of Bentheim sandstone under triaxial compression. Phys Chem Earth Part A Solid Earth Geodyn 26(1–2):21–25. doi:10.1016/S1464-1895(01)00017-5
41. Liu C, Pollard DD, Gu K, Shi B (2015) Mechanism of formation of wiggly compaction bands in porous sandstone: 2. Numerical simulation using discrete element method. J Geophys Res Solid Earth 120(12):8153–8168. doi:10.1002/2015JB012374
42. Liu Y, Sun W, Yuan Z, Fish J (2016) A nonlocal multiscale discrete-continuum model for predicting mechanical behavior of granular materials. Int J Numer Methods Eng 106(2):129–160. doi:10.1002/nme.5139
43. Ma X, Haimson BC (2016) Failure characteristics of two porous sandstones subjected to true triaxial stresses. J Geophys Res Solid Earth 121(9):6477–6498. doi:10.1002/2016JB012979
44. Marketos G, Bolton MD (2005) Compaction bands as observed in DEM simulations In: Proceedings of the 5th international conference on micromechanics of granular media, powders and grains, pp 1405–1408
45. Marketos G, Bolton MD (2007) A DEM study of compaction band formation. In: Bifurcations, instabilities, degradation in geomechanics. Springer, Berlin, pp 155–171
46. Marketos G, Bolton MD (2009) Compaction bands simulated in discrete element models. J Struct Geol 31(5):479–490. doi:10.1016/j.jsg.2009.03.002
47. Meier HA, Steinmann P, Kuhl E (2008) Towards multiscale computation of confined granular media-Contact forces, stresses and tangent operators. Tech Mech 16(1):77–88
48. Miehe C, Dettmar J, Zäh D (2010) Homogenization and two-scale simulations of granular materials for different microstructural constraints. Int J Numer Methods Eng 83(8–9):1206–1236. doi:10.1002/nme.2875
49. Mollema PN, Antonellini MA (1996) Compaction bands: a structural analog for anti-mode I cracks in aeolian sandstone. Tectonophysics 267(1–4):209–228. doi:10.1016/S0040-1951(96)00098-4
50. Nguyen TK, Combe G, Caillerie D, Desrues J (2014) FEM x DEM modelling of cohesive granular materials: numerical homogenisation and multi-scale simulation. Acta Geophys 62(3):1–18. doi:10.2478/s11600-013-00
51. Nitka M, Combe G, Dascalu C, Desrues J (2011) Two-scale modeling of granular materials: a DEM–FEM approach. Granul Matter 13(3):277–281. doi:10.1007/s10035-011-0255-6
52. Oda M (1982) Fabric tensor for discontinuous geological materials. Soils Found 22(4):96–108. doi:10.3208/sandf1972.22.4_96
53. Oka F, Kimoto S, Higo Y, Ohta H, Sanagawa T, Kodaka T (2011) An elasto-viscoplastic model for diatomaceous mudstone and numerical simulation of compaction bands. Int J Numer Anal Methods Geomech 35(2):244–263. doi:10.1002/nag.987
54. Olsson WA (1999) Theoretical and experimental investigation of compaction bands in porous rock. J Geophys Res 104(B4):7219–7228. doi:10.1029/1998JB900120
55. Olsson WA (2001) Quasistatic propagation of compaction fronts in porous rock. Mech Mater 33(11):659–668. doi:10.1016/S0167-6636(01)00078-3
56. Olsson WA, Holcomb DJ (2000) Compaction localization in porous rock. Geophys Res Lett 27(21):3537–3540. doi:10.1029/2000GL011723
57. Olsson WA, Holcomb DJ, Rudnicki JW (2002) Compaction localization in porous sandstone: implications for reservoir mechanics. Oil Gas Sci Technol 57(5):591–599. doi:10.2516/ogst:2002040
58. Park JW, Song JJ (2009) Numerical simulation of a direct shear test on a rock joint using a bonded-particle model. Int J Rock Mech Min Sci 46(8):1315–1328. doi:10.1016/j.ijrmms.2009.03.007
59. Potyondy DO, Cundall PA (2004) A bonded-particle model for rock. Int J Rock Mech Min Sci 41(8 SPEC.ISS.):1329–1364. doi:10.1016/j.ijrmms.2004.09.011
60. Rudnicki JW (2004) Shear and compaction band formation on an elliptic yield cap. J Geophys Res 109(B3):1–10. doi:10.1029/2003JB002633
61. Rudnicki JW, Rice JR (1975) Conditions for the localization of deformation in pressure-sensitive dilatant materials. J Mech Phys Solids 23(6):371–394. doi:10.1016/0022-5096(75)90001-0

62. Schultz RA, Okubo CH, Fossen H (2010) Porosity and grain size controls on compaction band formation in Jurassic Navajo Sandstone. Geophys Res Lett 37(22):1–5. doi:10.1029/2010GL044909
63. Sternlof KR, Rudnicki JW, Pollard DD (2005) Anticrack inclusion model for compaction bands in sandstone. J Geophys Res 110(B11):B11403. doi:10.1029/2005JB003764
64. Tembe S, Vajdova V, Wong T, Zhu W (2006) Initiation and propagation of strain localization in circumferentially notched samples of two porous sandstones. J Geophys Res 111(B2):B02409. doi:10.1029/2005JB003611
65. Tembe S, Baud P, Wong T (2008) Stress conditions for the propagation of discrete compaction bands in porous sandstone. J Geophys Res 113(B9):B09409. doi:10.1029/2007JB005439
66. Townend E, Thompson BD, Benson PM, Meredith PG, Baud P, Young RP (2008) Imaging compaction band propagation in Diemelstadt sandstone using acoustic emission locations. Geophys Res Lett 35(15):1–5. doi:10.1029/2008GL034723
67. Vajdova V, Wong TF (2003) Incremental propagation of discrete compaction bands: acoustic emission and microstructural observations on circumferentially notched samples of Bentheim. Geophys Res Lett 30(14):1775–1778. doi:10.1029/2003GL017750
68. Wang B, Chen Y, Wong T (2008) A discrete element model for the development of compaction localization in granular rock. J Geophys Res 113(B3):B03202. doi:10.1029/2006JB004501
69. Wang K, Sun W (2016) A semi-implicit discrete-continuum coupling method for porous media based on the effective stress principle at finite strain. Comput Methods Appl Mech Eng. doi:10.1016/j.cma.2016.02.020
70. Wang Y-H, Leung S-C (2008) A particulate-scale investigation of cemented sand behavior. Can Geotech J 45(1):29–44. doi:10.1139/T07-070
71. Wong T, Szeto H, Zhang J (1992) Effect of loading path and porosity on the failure mode of porous rocks. Appl Mech Rev 45(8):281–293. doi:10.1115/1.3119759
72. Wong T-F, David C, Zhu W (1997) The transition from brittle faulting to cataclasic flow in porous sandstones: mechanical deformation. J Geophys Res 102(B2):3009–3025
73. Wong TF, Baud P (1999) Mechanical compaction of porous sandstone. Oil Gas Sci Technol 54(6):715–727. doi:10.2516/ogst:1999061
74. Wong TF, Baud P, Klein E (2001) Localized failure modes in a compactant porous rock. Geophys Res Lett 28(13):2521–2524. doi:10.1029/2001GL012960
75. Zhang J, Wong T-F, Davis DM (1990) Micromechanics of pressure-induced grain crushing in porous rocks. J Geophys Res 95(B1):341. doi:10.1029/JB095iB01p00341
76. Zhao J, Guo N (2015) The interplay between anisotropy and strain localisation in granular soils: a multiscale insight. Géotechnique 65(8):642–656. doi:10.1680/geot.14.P.184
77. Zheng Z, Sun WC, Fish J (2016) Micropolar effect on the cataclastic flow and brittle–ductile transition in high-porosity rocks. J Geophys Res B Solid Earth 121(3):1425–1440. doi:10.1002/2015JB012179